

**Large-scale natural fracture network patterns  
Insights from automated mapping in the Lilstock (Bristol Channel) limestone outcrops**

Prabhakaran, Rahul; Urai, J. L.; Bertotti, G.; Weismüller, C.; Smeulders, D.M.J.

**DOI**

[10.1016/j.jsg.2021.104405](https://doi.org/10.1016/j.jsg.2021.104405)

**Publication date**

2021

**Document Version**

Final published version

**Published in**

Journal of Structural Geology

**Citation (APA)**

Prabhakaran, R., Urai, J. L., Bertotti, G., Weismüller, C., & Smeulders, D. M. J. (2021). Large-scale natural fracture network patterns: Insights from automated mapping in the Lilstock (Bristol Channel) limestone outcrops. *Journal of Structural Geology*, 150, Article 104405. <https://doi.org/10.1016/j.jsg.2021.104405>

**Important note**

To cite this publication, please use the final published version (if applicable).  
Please check the document version above.

**Copyright**

Other than for strictly personal use, it is not permitted to download, forward or distribute the text or part of it, without the consent of the author(s) and/or copyright holder(s), unless the work is under an open content license such as Creative Commons.

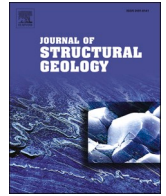
**Takedown policy**

Please contact us and provide details if you believe this document breaches copyrights.  
We will remove access to the work immediately and investigate your claim.



Contents lists available at ScienceDirect

## Journal of Structural Geology

journal homepage: [www.elsevier.com/locate/jsg](http://www.elsevier.com/locate/jsg)

# Large-scale natural fracture network patterns: Insights from automated mapping in the Lilstock (Bristol Channel) limestone outcrops

Rahul Prabhakaran<sup>a,b,\*</sup>, J.L. Urai<sup>d</sup>, G. Bertotti<sup>a</sup>, C. Weismüller<sup>c</sup>, D.M.J. Smeulders<sup>b</sup>

<sup>a</sup> Department of Geoscience and Engineering, Delft University of Technology, Delft, the Netherlands

<sup>b</sup> Department of Mechanical Engineering, Eindhoven University of Technology, Eindhoven, the Netherlands

<sup>c</sup> Neotectonics and Natural Hazards, RWTH Aachen University, Aachen, Germany

<sup>d</sup> Structural Geology, Tectonics and Geomechanics, RWTH Aachen University, Aachen, Germany

## ARTICLE INFO

## Keywords:

Fractured pavements  
Natural fracture networks  
Carbonates  
Spatial graphs  
Graph theory  
Discrete fracture networks

## ABSTRACT

The Lilstock outcrop in the southern Bristol Channel provides exceptional exposures of several limestone beds displaying stratabound fracture networks, providing the opportunity to create a very large, complete, and ground-truthed fracture model. Here we present the result of automated fracture extraction of high-resolution photogrammetric images (0.9 cm/pixel) of the full outcrop, obtained using an unmanned aerial vehicle, to obtain a spatially extensive, full-resolution map of the complete fracture network with nearly 350,000 ground-truthed fractures. We developed graph-based functions to resolve some common issues that arise in automatic fracture tracing such as incomplete traces, incorrect topology, artificial fragmentation, and linking of fracture segments to generate geologically significant trace interpretations. The fracture networks corresponding to different regions within the outcrop are compared using several network metrics and the results indicate both inter- and intra-network (layer to layer) structural variabilities. The dataset is a valuable benchmark in the study of large-scale natural fracture networks and its extension to stochastic network generation in geomodelling. The dataset also highlights the intrinsic spatial variation in natural fracture networks that can occur even in weakly-deformed rocks over relatively short length scales of tens of metres.

## 1. Introduction

Fractures in rocks can form networks with fracture tips forming abutting or crossing physical interactions with other fractures or remaining isolated within rock matrix. The evolution into a final cumulative network pattern is history-dependent. The pattern evolves depending upon how loading paths and rock properties governing growth affect propagation rates under episodic conditions when failure criteria are met, in addition to the superposed effects of pre-existing sets (Laubach et al., 2019). The spatial arrangements of fracture networks can be a significant geomorphic agent, influencing landscape evolution processes (Scott and Wohl, 2019), serve as dissolution pathways for karstic cave formation (Boersma et al., 2019; Bertotti et al., 2020), and influence subsurface fluid flow patterns that are relevant for hydrogeological, geo-energy and waste disposal applications (National Research Council, 1996; Berkowitz, 2002). Given such non-trivial influences, it is important to be able to characterize large-scale fracture patterns from a network perspective.

Mechanistic numerical modelling of fracture propagation and subsequent fracture network formation can include complex physics pertaining to individual fractures such as fracture tip behaviour, fluid driven fracturing, interaction of propagating fractures with pre-existing discontinuities and other propagating fractures (Laubach et al., 2019). Such mechanistic models can be based on extended finite element methods (such as Remij et al., 2015; Valliappan et al., 2019 etc), discrete element methods (such as Virgo et al., 2016; Guo et al., 2017 etc), and phase-field methods (such as Yoshioka and Bourdin, 2016; Lepillier et al., 2020 etc), and differ in the way rock substrate and propagating fracture are numerically treated. Such complex models are computationally intensive and are limited in the spatial extent of network evolution. Recent developments include approaches in which fracture networks genetically evolve from flaws without resorting to rigorous geomechanical treatment (such as Lavoine et al., 2020; Welch et al., 2019) but large-scale network development is still difficult to realize.

In such a context, outcrop-derived networks hold relevance. The advantage of outcrops is that they implicitly encode spatial organization

\* Corresponding author. Department of Mechanical Engineering, Eindhoven University of Technology, Eindhoven, the Netherlands.

E-mail address: [R.Prabhakaran@tudelft.nl](mailto:R.Prabhakaran@tudelft.nl) (R. Prabhakaran).

<https://doi.org/10.1016/j.jsg.2021.104405>

Received 14 March 2021; Received in revised form 18 June 2021; Accepted 24 June 2021

Available online 30 June 2021

0191-8141/© 2021 The Author(s). Published by Elsevier Ltd. This is an open access article under the CC BY license (<http://creativecommons.org/licenses/by/4.0/>).

of networks and network properties can be observed and sampled when outcrop quality permits. The proliferation of Unmanned Aerial Vehicle (UAV) photogrammetry has led to an increase in both volumes and speed of acquisition of digital outcrop data (Bemis et al., 2014; Hodgetts, 2013). Coupled with automatic image processing tools, it is now possible to obtain outcrop-derived 2D discrete fracture networks (DFNs) at large enough scales to enhance our understanding of geometrical organization and spatial heterogeneity in natural fracture networks (Palamakumbura et al., 2020).

Outcrop-based characterization of natural fractures typically involves fracture sampling methods such as the use of scanlines (for e.g. Priest and Hudson, 1981; Mauldon et al., 2001; Rohrbaugh et al., 2002), fracture traces from orthorectified fractured rock images (for e.g. Bistacchi et al., 2015; Bisdorn et al., 2017), fracture traces from LIDAR (for e.g. Lamarche et al., 2011; Wilson et al., 2011), and geophysical imaging such as ground penetrating radar (such as Day-Lewis et al., 2017; Molron et al., 2020). Recent advances in fracture characterization utilize data-fusion techniques in which multi-spectral, hyperspectral, gravity, and magnetic remote sensing are combined in outcrop studies. The combination of these techniques incorporates high-degrees of geological realism. In this contribution, the focus and scope is on the mapping of 2D fracture traces using UAV photogrammetry at the Lilstock outcrop, Bristol Channel, UK which exposes multiple fractured limestone beds.

We continue upon the first (Weismüller et al., 2020a,b) and second (Passchier et al., 2021) part of this project. The complex shearlet transform method (Reisenhofer et al., 2016; Prabhakaran et al., 2019) is used to automatically extract fracture traces from high resolution photogrammetric data published by Weismüller et al. (2020a,b). A critical comparison between automatic and manual tracing was presented in Weismüller et al. (2020a,b) using topological relationships, fracture intensity, and fracture density measures, and showed that the quality of automatic tracing is consistent with the interpretations of a proficient interpreter. Weismüller et al. (2020a,b) covered five regions of 140 sq. m each within the Lilstock pavement while Passchier et al. (2021) has mapped the different fracture generations but incompletely.

In this work, the automatic tracing is extended to an area that is 20 times larger resulting in a rich dataset that amounts to nearly 800,000 fracture segments. We develop a set of graph-based programmatic routines that convert automatically extracted fracture segments into geologically significant fracture traces. The areal extent, detail, and spatial continuity of the resultant fracture network data, comprising of around 350,000 fractures, is unique. The dataset is an important benchmark which provides a means to overcome sampling and truncation effects typically experienced with small fractured outcrops and which have so-far limited efforts at fracture characterization.

## 2. Fractures as spatial graphs

Graph theory concerns the study of mathematical structures, *graphs*, that model pairwise relations between objects. The use of graph theory and spatial graph representations to represent fracture networks was suggested by authors such as Adler and Thovet (1999), Manzo (2002), Valentini et al. (2007a), Valentini et al. (2007b), Santiago et al. (2016), and Sanderson et al. (2019). Such a graph representation maintains topological relationships between fracture segments and spatial relationships between fracture edges. Topology serves as a means to quantify connectivity of a fracture network. Network connectivity parameters have important implications for fractured hydrogeologic and subsurface modelling (Berkowitz, 2002). In addition to topological relationships, fracture networks are also spatial in nature. In this regard, fracture networks are similar to roads and power grids in that the networks are embedded in space. Such families of spatial networks are observed to have steric constraints that impose limitations on the maximum degree of a node (Barthelemy, 2018). Many specialized methods and techniques developed for spatial graphs can, therefore, be applied to fracture network data.

Graphs are typically represented in matrix forms, allowing the use of computational linear algebra techniques and algorithms to investigate properties of the network structure, and derive insights into spatial and spectral properties. Within the structural geology literature, such approaches are not widespread as data pipelines that can deliver sufficient volumes of fracture data in the form of spatial graphs face several challenges in data acquisition and processing. The advent of UAV-based data acquisition and automatic fracture trace extraction opens up new avenues to use graph algorithms to extract insights from large-scale fracture patterns.

From graph theory, a *graph* is a pair  $G = (V, E)$  with  $V$  being a set of *vertices* and  $E$ , a set of *edges*. The abstraction that connects mathematical graph theory to fracture networks is that fracture intersections form the vertex set,  $V$  and fracture segments linking the vertex set  $V$  form the edge set,  $E$ . When a spatial positioning data structure is additionally specified to represent position of each fracture intersection in 2D cartesian space, the fracture network forms the planar graph,  $G_p$ . An example of a fracture network in the form of a graph, with edges representing fracture segments and vertices denoting fracture intersections is depicted in Fig. 1(a). This is a simple planar drawing where nodes are positioned in such a way that there are no edge crossings. The graph has 1746 nodes and 2617 edges. The same graph with spatial positioning is depicted in Fig. 1(b).

In this representation, the definition of a geological fracture ' $F$ ', is simply a subset of ' $n$ ' nodes within the graph. This is also equivalent to a subset of ' $n - 1$ ' connected edges which are contained within the edge set that forms a walk or path within the graph (see Fig. 1(c) and (d)). The entire fracture network is a list of paths which are specific sequences of nodes (and edges). A *weighted* graph is one in which the edge set is associated with weights that can represent, for instance, the relative importance of edges within the complete edge list. In case of fracture networks, this may simply be the euclidean distance between the end nodes of the particular edge. A graph may be *directed* and referred to as a *digraph* which implies that an edge has a source node and a target node. In case of fracture networks, an *undirected* graph representation is sufficient.

The graph representation where fracture intersections form vertices and fracture segments form edges, as depicted in Fig. 1(b), is called the *primal* form (Barthelemy, 2018). There is also a *dual* form of a graph in which fractures from tip-to-tip form graph nodes and interconnections between fractures form the edges (Barthelemy, 2018). Such *dual* representations have been used by Adler and Thovet (1999), Valentini et al. (2007b), Andresen et al. (2013), and Vevatne et al. (2014) for fracture networks. To illustrate the difference between the two representations, an example network from Bisdorn et al. (2017) is depicted in the primal form in Fig. 2(a) with fracture intersections being the vertices and fracture segments forming the edges. The dual form where fractures from tip-to-tip are nodes and intersections between fractured are edges is depicted in Fig. 2(b). It can be observed that the longest fracture striking NW-SE has the maximum number of intersections with smaller fractures abutting on to or crossing it. The longest fracture is therefore the node with the highest degree in the dual graph. Since the dual representation considers only topological connections between fractures from tip-to-tip, we do not associate any spatial position to the nodes in Fig. 2(b). Fig. 2(c) and Fig. 2(d) depict adjacency matrices of the primal and dual graphs respectively. The degree of a node denotes the number of edges that intersect the particular node. The node degree distributions of the primal and dual are depicted in Fig. 2(e) and (f) respectively. The node degrees in the primal are subject to geometric constraints with a maximum degree of 6 (a hexa type joint). The dual graph degree distribution is more spread out with 64 being the largest degree.

By converting fracture network shapefiles to primal graphs, we can then use graph algorithms and metrics to analyze the networks. Various network metrics can be used to quantify inter- and intra-network variability in fracture networks using the graph representation. This is a novel approach in fracture network analysis in the Geosciences, made

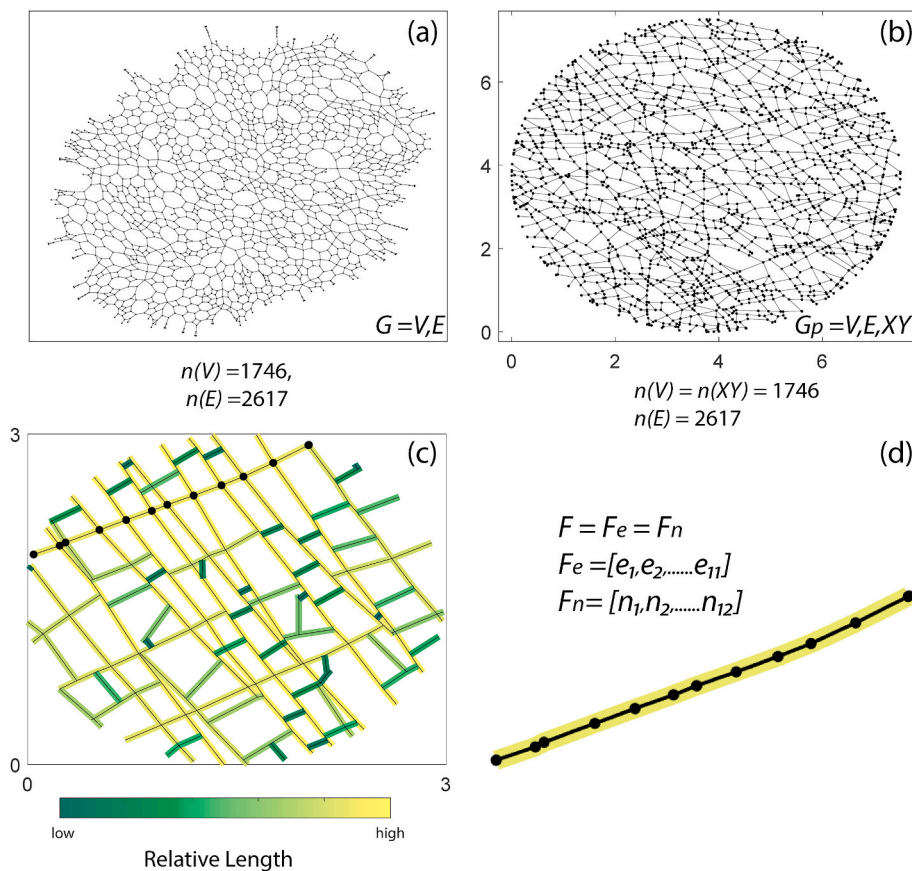


**Fig. 1.** A graph with no spatial positioning can be simply depicted as nodes and edges with a method of planar drawing (Nishizeki and Rahman, 2004). Here a fracture network is converted to a graph and drawn in a “gravity” layout. (b) The fracture graph with spatial positioning applied to each of its nodes (dimensions in metres) (c) An example of a fracture network plotted as a spatial graph with individual fractures from tip-to-tip colour coded based on fracture length (dimensions in metres). One fracture is highlighted with enlarged nodes (d) enlarged view of a single fracture ‘F’ within a spatial graph, defined as a set of ‘n’ nodes or ‘n – 1’ edges. (For interpretation of the references to colour in this figure legend, the reader is referred to the Web version of this article.)

possible by the large amount of fractures. We propose that our results form a valuable benchmark for future fracture mapping and characterization methods, and provide the mapped fractures for further study. The network data and the code used is available as supplements with this contribution for the benefit of researchers interested in natural fracture characterization.

### 3. Geology of the study area

The outcrops studied in this paper are located off the southern coast of the Bristol Channel in West Somerset, UK, close to the hamlet of Lilstock (see Fig. 3). The area is within a 7.428 sq.km geological Site of Special Scientific Interest (SSSI), referred to as the Blue Anchor to Lilstock Coast SSSI, due to the exposures ranging from Early Jurassic to Lower Lias. Deformation features such as faults, fractures, and joints are exposed within the study area (Spruženiece et al., 2020). The site is well-studied in terms of structural features, tectonic history, sedimentology, stratigraphy, and basin evolution (for e.g., Kamerling, 1979; Van Hoorn, 1987; Nemčok et al., 1995; Rawnsley et al., 1998; Kelly et al., 1999; Peacock, 2004; Glen et al., 2005; Engelder and Peacock, 2001; Belayneh et al., 2006). The regions of interest and the focus of this contribution are three fractured limestone pavements referred to as benches by Loosveld and Franssen (1992).

The fractured pavements correspond to the northern limb of a single E-W trending anticline formed due to N-S compression during the Tertiary (Dart et al., 1995). We focus on five fractured pavements the extent of which is depicted in Fig. 3. The fractured regions are designated as Areas 1–5. Areas 1 & 3 and Areas 2 & 4 belong to the same stratigraphic layer. The particular areas were chosen as they are largely devoid of vegetation and weathering, and contain joints belonging to different stages in the tectonic history forming a well-connected spatial network. Additionally, the studied regions contain sub-regions which were the

focus of previous work by Loosveld and Franssen (1992), Rawnsley et al. (1998), Engelder and Peacock (2001), Belayneh and Cosgrove (2004), Belayneh (2004), and Gillespie et al. (2011). The relationship between joints described in the above-mentioned works is discussed by Passchier et al. (2021).

#### 3.1. Structural history

The structural history of the region may be classified into several tectonic phases. Beginning with N-S extension in the Early Jurassic to Early Cretaceous and again in the Late Cretaceous to Oligocene (Rawnsley et al., 1998), these events are evidenced by E-W striking normal faults (Brooks et al., 1988). These extension events were followed by N-S Alpine compression during the late Oligocene to Miocene resulting in inversion of normal faults and gentle folding, followed by progressive relaxation during the Late or post-Miocene (Rawnsley et al., 1998). Normal faults and conjugate strike slip faults indicate this event (Dart et al., 1995; Glen et al., 2005; Kelly et al., 1999; Nemčok et al., 1995). This was followed by burial of up to 1.5 km and exhumation with features such as small folds, faults, veins, and joints (Rawnsley et al., 1998; Hancock and Engelder, 1989).

#### 3.2. Previous descriptions of jointing

The Mode-I joints exposed in the Lilstock are bedding-perpendicular and largely stratabound with apertures enhanced by tide-induced dissolution, ranging from sub-millimeter at the bottom to an order of centimetres at the bed top (Gillespie et al., 2011). The decimeter thick limestone layers are intercalated with claystone layers of the order of  $10^0 - 10^2$  cm thicknesses. A striking feature of the jointing is the network that is formed due to joints abutting or crossing each other. The presence of small displacement faults within the bench cause visibly

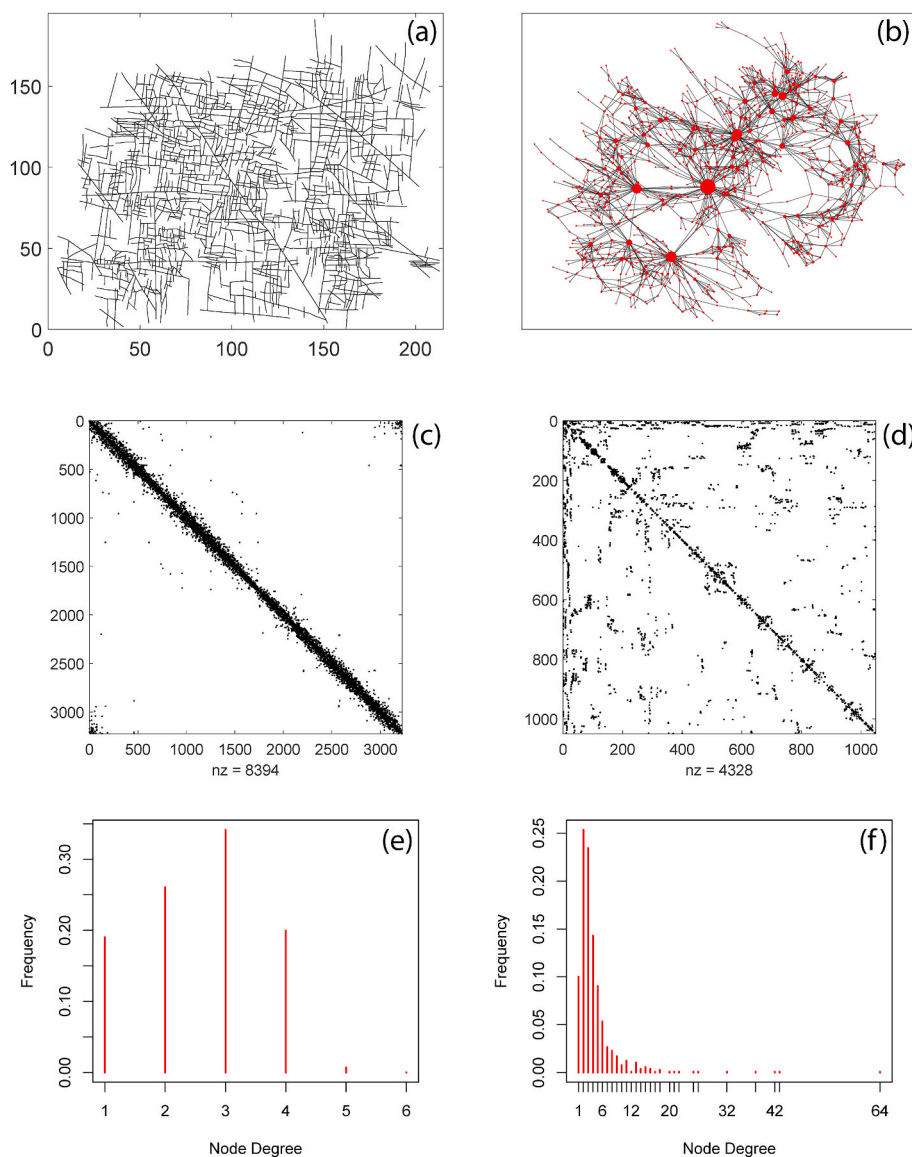


**Fig. 2.** (a) Primal graph representation of a manually interpreted fracture network, Apodi-4, from [Bisdorn et al. \(2017\)](#) in the Jandaira formation of the Potiguar Basin, Brazil having 3309 nodes and 4258 edges. Only the largest connected component of the network is depicted after removing all isolated fractures. (b) Dual graph representation of the Apodi-4 fracture network using a ‘force’ layout. Fracture traces from tip-to-tip are represented as graph nodes and intersections between fractures are considered as edges. The dual representation has 2172 edges and 1082 nodes. Node sizes are plotted proportional to the node degrees and highlights the centrality of the relatively few long fractures (c) Adjacency matrix of primal graph (d) Adjacency matrix of dual graph (e) Degree histogram representing node topology of primal graph (f) Degree histogram representing node topology of dual graph.

identifiable variations in fracture patterns and intensities. The Lilstock outcrop also contains several long, fan-shaped joints that emanate from asperities on faults ([Rawnsley et al., 1998](#)). These joint fans have also been described in other outcrops near the Bristol Channel in similar lithologies ([Bourne and Willemsse, 2001](#)).

The joints are believed to be due to minor tectonic events that post-dated the stress inversion. Various authors have interpreted jointing histories and number of joint sets based on observations within sub-regions of the outcrop. [Loosveld and Franssen \(1992\)](#) identified six joint sets based on orientation. [Rawnsley et al. \(1998\)](#) identified four main joint sets using characteristics such as orientation, length, and spacing. [Engelder and Peacock \(2001\)](#) identified six jointing sets based on orientation and abutting criteria. [Belayneh \(2004\)](#) identified six joint sets based on orientation, length, and aperture. More recent work by [Wyller \(2019\)](#) distinguished ten jointing generations using abutting relationships, length, and orientation. These above-mentioned attempts at delineating jointing generations are limited to certain regions within the entire outcrop (see [Fig. 3](#)). [Passchier et al. \(2021\)](#) utilized the same image dataset as ours and was able to identify eight generations of joints from manually traced fractures that include all regions covered by the previous studies. The criteria used by [Passchier et al. \(2021\)](#) to partition individual fractures into jointing generations consisted of combination

of length, orientation, and abutting criteria. The results highlighted considerable spatial variability in jointing with some regions containing just 2–3 generations while other areas achieved saturation with the maximum eight sets.

[Rawnsley et al. \(1998\)](#) associate the earliest joint sets as forming sub-parallel to regional Alpine compression, with subsequent jointing sets being perturbed by faults and influenced by anticlockwise shift of maximum horizontal stress during basin-wide relaxation of Alpine compression. The youngest joints were proposed to be correlated with relaxation or contracting of rock. [Engelder and Peacock \(2001\)](#) suggested that joint formation is linked to minor tectonic events postdating the basin inversion. The youngest joints are proposed to be correlated with the contemporary stress field ([Engelder and Peacock, 2001](#)) or due to exhumation in a late stage of the Alpine stress field ([Hancock and Engelder, 1989](#)). [Dart et al. \(1995\)](#) proposed that the jointing patterns involve overprinting of joint generations.

## 4. Methods

### 4.1. Photogrammetric dataset

The image data that we consider in this work is extracted from UAV-

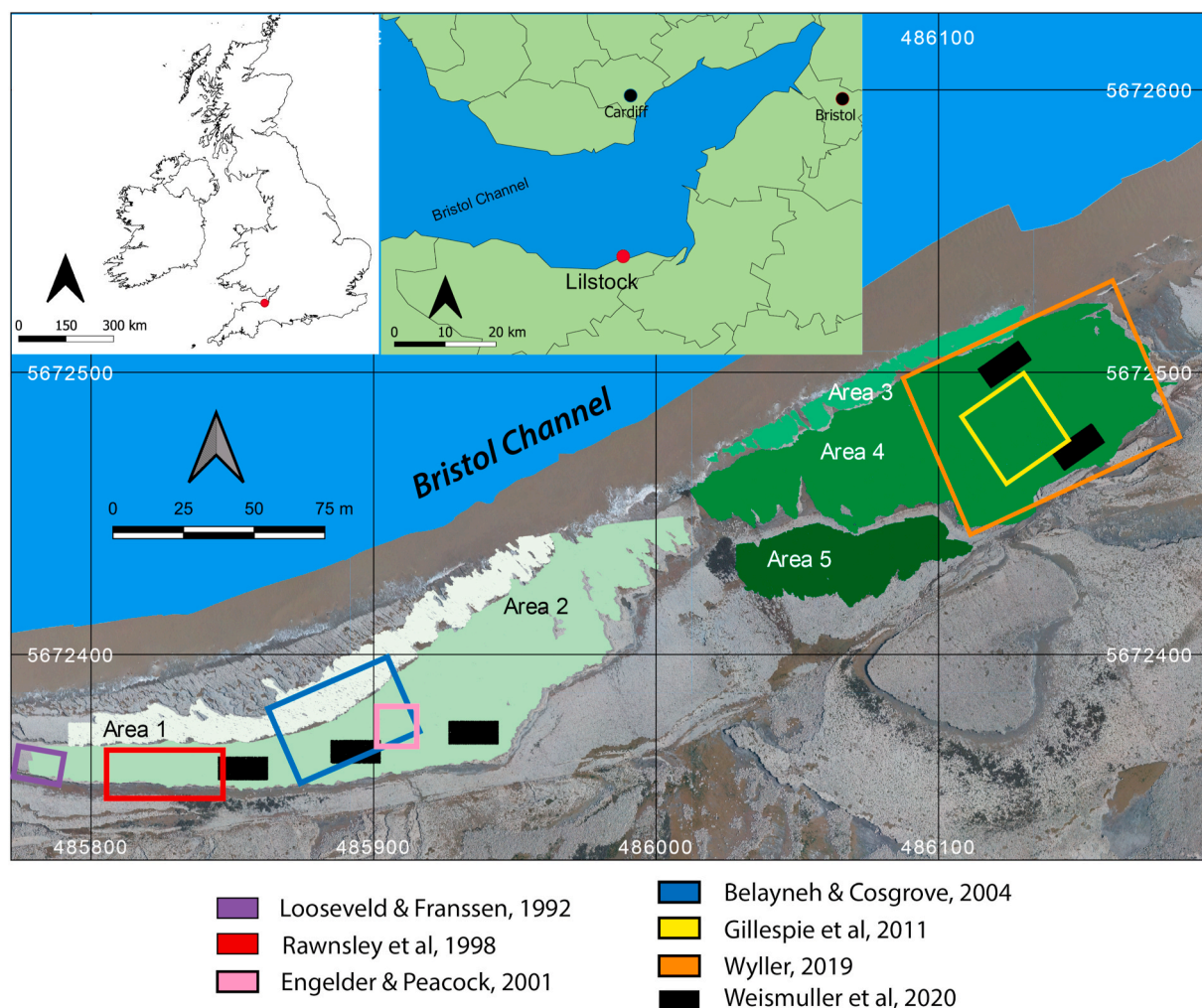


**Fig. 3.** Overview of the study area located at Lilstock, Bristol Channel, UK generated from UAV photogrammetry at an altitude of 100 m. The orthomosaic is available as an open dataset (Weismüller et al., 2020a,b). Spatial extent of five areas within the Bristol Channel outcrop where fracture networks are automatically extracted is depicted in sequential shades of green. Approximate areas where previous studies done within the same outcrop are also highlighted. (Shapefiles of UK regional boundaries used to create inset images is obtained from <https://geoportal.statistics.gov.uk/> available under an Open Government Licence v3.0.). (For interpretation of the references to colour in this figure legend, the reader is referred to the Web version of this article.)

derived orthomography published as a dataset (Weismüller et al., 2020a, b). The full dataset comprises of orthomosaics generated from UAV flights at 10 m, 20 m, 25 m, and 100 m. We utilize the orthomosaics acquired between 20 and 25 m flight altitude resulting in imagery of 0.9 cm/pixel. Weismüller et al. (2020a,b) used this value of resolution to manually interpret fractures in five 140 sq.m regions within Areas 2 and 4 (see Fig. 3). Weismüller et al. (2020a,b) also performed automatic interpretation in the five regions using the complex shearlet transform method (Prabhakaran et al., 2019) and quantitatively compared with manual interpretations. The validation of manual with respect to automatic mapping indicated closely similar fracture patterns, generating confidence in an endeavour to extend the automatic interpretation to larger regions of the outcrop over multiple layers. Passchier et al. (2021) used the same image dataset with similar resolution to identify jointing generations from manual interpretations within Areas 2 and 4.

#### 4.2. Automatic tracing workflow

The complex-shearlet transform (Reisenhofer et al., 2016) was extended to automatic outcrop-scale fracture trace extraction from UAV photogrammetry by Prabhakaran et al. (2019). The workflow comprises of a series image processing steps which is depicted in Fig. 4. The steps include complex shearlet-based ridge detection, thresholding,

skeletonization and polyline fitting. The image data is divided into sub-tiles of 1000 x 1000 pixels for efficient computation and considering memory requirements. The processing steps are then applied to each tile separately. This splitting of the images therefore enables processing on multiple workstations. The realized vector geometries are combined into shapefiles. The number of image tiles that correspond to each bench is summarized in Table .1 along with approximate areal extent.

Since quality of automatic fracture detection depends on enlarged discontinuities owing to weathering or otherwise and given that the degree of weathering is spatially variable, a single set of parameters is insufficient to efficiently extract all exposed traces. Therefore, three different sets of shearlet parameters are used for ridge detection yielding three different ridge image ensembles ( $E1$ ,  $E2$ ,  $E3$ ) that capture fractures both subtle and well-eroded. The three shearlet system parameters used are listed in the data supplement. Various linear combinations ( $a$ ,  $b$ ,  $c$ ) are applied to  $E1$ ,  $E2$ ,  $E3$  to obtain an optimal  $E_{final}$  for each image tile as per.

$$E_{final} = aE1 + bE2 + cE3.$$

This combined ensemble,  $E_{final}$  is then used for further image processing as per the workflow in Fig. 4. The traces extracted from each image tile is then merged as a single shapefile. An example of an image tile with a ridge ensemble and the corresponding vectorized shapefile is depicted in Fig. 5. Though the Lilstock outcrop is a high-quality

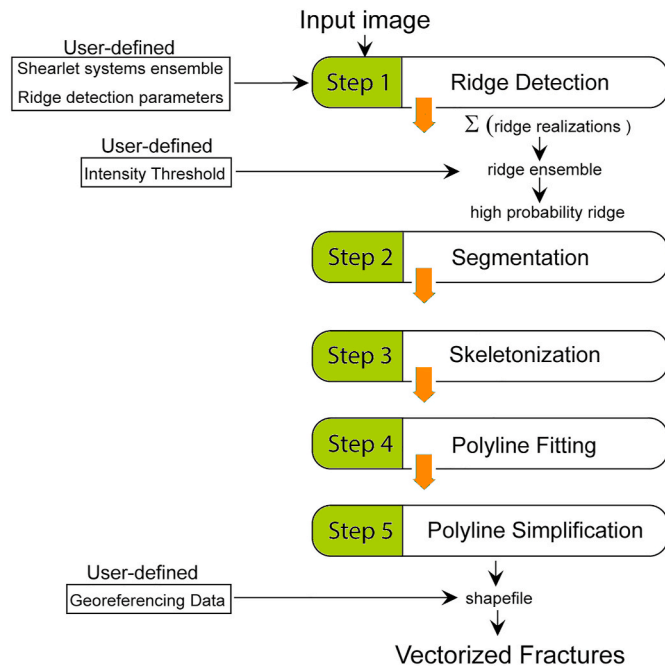


**Fig. 4.** Automatic detection workflow used to convert UAV photogrammetric images to fracture traces used previously in Prabhakaran (2019) and Weismüller et al. (2020a,b).

**Table 1**  
Study areas and approximate area covered.

Region	Image tiles	Approx. area (sq.m)
Area 1	58	2034
Area 2	128	6017
Area 3	25	714
Area 4	107	6749
Area 5	34	1473

exposure, there are still sources of false positives owing to erosion, water puddles, shrubbery, and rubble. These artefacts are removed manually using interactive GIS tools. The total time taken for automatic mapping for all tiles was 384 h CPU time (using an Intel Xeon processor with 4 cores, 3.5 GHz, and 32 GB RAM). The time taken to clear the artefacts varies between 1 and 2 h per image tile depending upon the image.

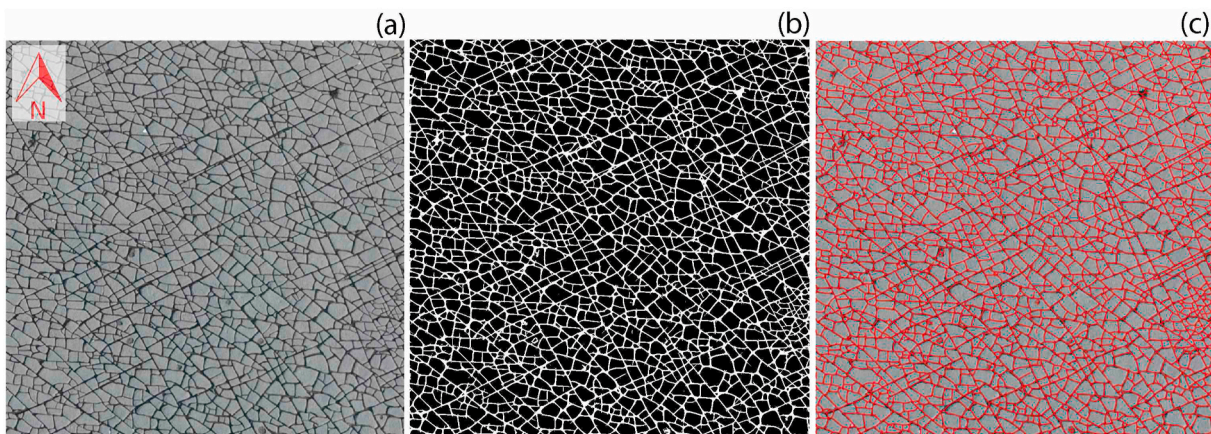


**Fig. 5.** An image tile (9.3 × 9.3 m) from the Bristol Channel dataset (b) computed ridge ensemble (c) the vectorized shapefile overlain on the image.

### 4.3. Shapefiles to graphs

The automatic traces are in the form of shapefiles. We developed MATLAB routines to enable conversion of shapefiles of fracture networks into graph data structures and vice-versa. The conversion results in a primal graph, which can then be converted to a dual graph if the sequence of primal graph edges that correspond to a complete fracture from tip-to-tip can be specified. The graph representations can then be exported in various graph formats that are readable by graph visualization software and packages such as Gephi (Bastian et al., 2009), iGraph (Csardi and Nepusz, 2006), and NetworkX (Hagberg et al., 2008).

### 4.4. Making graph representations geologically meaningful

The use of automatic tracing may produce fractures that deviate from a manual interpretation. When interpreting by hand, an interpreter utilizes multiple cues to trace a fracture from tip-to-tip and identify fracture tip topologies. Therefore, using ubiquitous network metrics such as cumulative length distributions, rose plots, topological summaries on automatically extracted traces can result in skewed results. To this end, we developed a series of graph manipulation routines that take the raw graph data input generated from the automatic traces into geologically meaningful data. This workflow is summarized in Fig. 6 and further described in the following sections. The code supplement contains the implementations of the functions.

#### 4.4.1. Topological discontinuities

Automatically traced interpretations can contain topological discontinuities. By analysing automatically-traced networks and comparing them with manual interpretations, we classify connectivity issues and design specific routines to resolve these discontinuities. The three most common topological errors are depicted in Fig. 7. These include situations when.

- a degree-1 node is in close proximity to a degree-2 node with near orthogonal angles
- a degree-3 (or Y-node) is present as three closely spaced degree-1 nodes
- two degree-2 nodes with sharp orthogonal angles are in close proximity

In order to resolve these topological errors in connectivity, we perform a delaunay triangulation (De Berg et al., 2000) on the fracture spatial graphs using the nodes as control points. The triangulation creates tri-elements around the fracture traces. By inspecting the histograms of tri-element areas, anomalous elements with very small areas

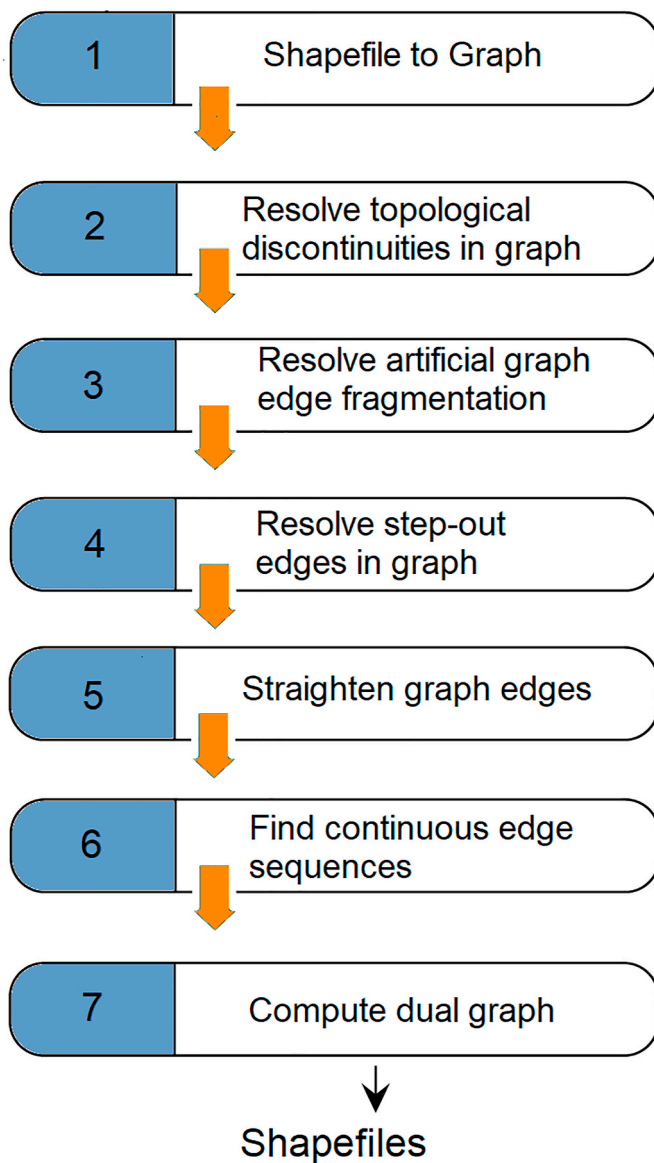


Fig. 6. Sequence of graph manipulation routines to convert shapefiles of automatically traced fracture segments to geologically significant fracture traces and dual graph representations.

can be isolated. These small tri-elements are formed at the regions of topological errors or with very high aspect ratios. Using a suitable cut-off area that is determined by visual inspection of the small tri-element areas, graph manipulations are performed on the graphs that resolve the loss of connectivity depending upon the node types and edge properties involved. The manipulations involve adding/removing edges and

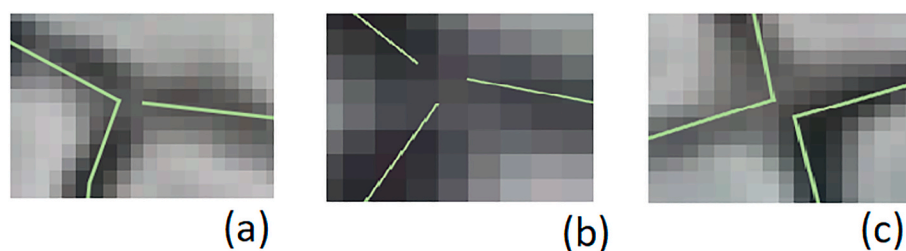


Fig. 7. Common topological errors caused by automatic detection (a) a degree-3 connection inaccurately traced as a degree-2 node with two nearly orthogonal edges in close proximity to a degree-1 node (b) a degree-3 connection incorrectly traced as three degree-1 nodes in close proximity (c) two degree-2 nodes with nearly orthogonal edges that are disconnected.

nodes and updating the fracture graph. The three types of manipulations that are done to rectify topological discontinuities are illustrated in Fig. 8. The code implementations are attached within the code supplement.

#### 4.4.2. Resolving artificial fragmentation of fracture segments

Artificial fragmentation of fracture trace happens when traces appear to be connected and topologically correct to visual inspection but split and saved separately within the shapefile attribute tables. This kind of situation can happen due to tile-wise image processing where fracture polylines that are otherwise continuous, are fragmented and saved as a cascade of isolated segments. Other reasons are due to the way polylines are fitted to skeletonized, binary pixel clusters as per the workflow in Fig. 4. The skeletonization procedure specifies branch points between intersecting fractures. However, due to varying ridge thickness within the image, it is sometimes possible that segments are connected but incorrectly labelled from a geological perspective. Such a situation is depicted in Fig. 9(a).

In order to be geologically consistent, the visually continuous but disconnected segments have to be combined into a single polyline entity. We develop a graph edge linking function that first identifies all degree-2 nodes within the graph. For these nodes, node neighbours with degree 2 are identified and appended into a preliminary node path. The end nodes of the node path are queried again for further neighbour nodes having degree-2 and repeated till there are no more such nodes in either direction of the node path. The resulting node path is now a single connected polyline representing a fracture segment. The implementation is attached within the code supplement. The effect of the edge linking is depicted in Fig. 9(b).

#### 4.4.3. Resolving step-outs

Automatically identifying fracture edges that belong to a single, continuous fracture from tip-to-tip is a task that can face complications due to the presence of step-outs or edges that have degree-3 (or Y-nodes) on either ends. Such Y-Y motifs often form *step-outs* which impede continuous path finding as they may strike in a different direction as that of longer adjacent edges. They turn out to be bottlenecks when we seek to identify long and continuous paths using segment strike as a search attribute. Examples of such step-out edges are shown in Fig. 10(a) and (c). To resolve the issue, we specifically filter for graph edges that are below a certain length threshold that have a degree of 3 on both start and terminating ends. Below a certain length threshold corresponding to the resolution of the image, a *merge* operation can be carried out deleting the step-out and creating a degree-4 node (see Fig. 10(b)) after adding three edges and removing one node. In our case we found that a value of around 1–2 times the image resolution was sufficient for the merge operations.

Above this length threshold, it is likely that the topology at either end of the step-out is correct, but the Y-Y edge needs to be *flattened* to correspond with the strike angle of one pair of edges on either side (see Fig. 10(d)). In this case, merging of the step-out may incorrectly displace some edges of the spatial graph. In this procedure, the edges that are



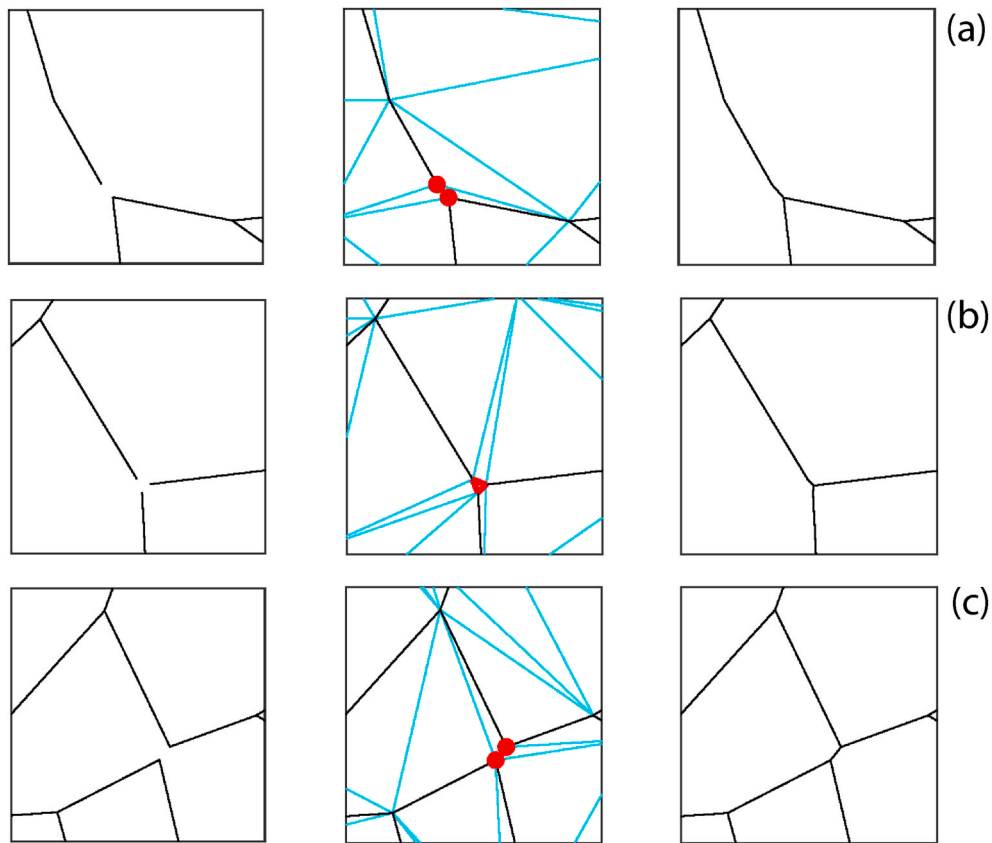


**Fig. 8.** Detail of rectification of the three types of topological discontinuities using Delaunay triangulation (a) type-1 discontinuity with degree-1 node in close proximity to a sharp-angled degree-2 node (b) type-2 discontinuity with three degree-1 nodes in close proximity (c) type-3 discontinuity with two degree-2 nodes having sharp angles in close proximity.

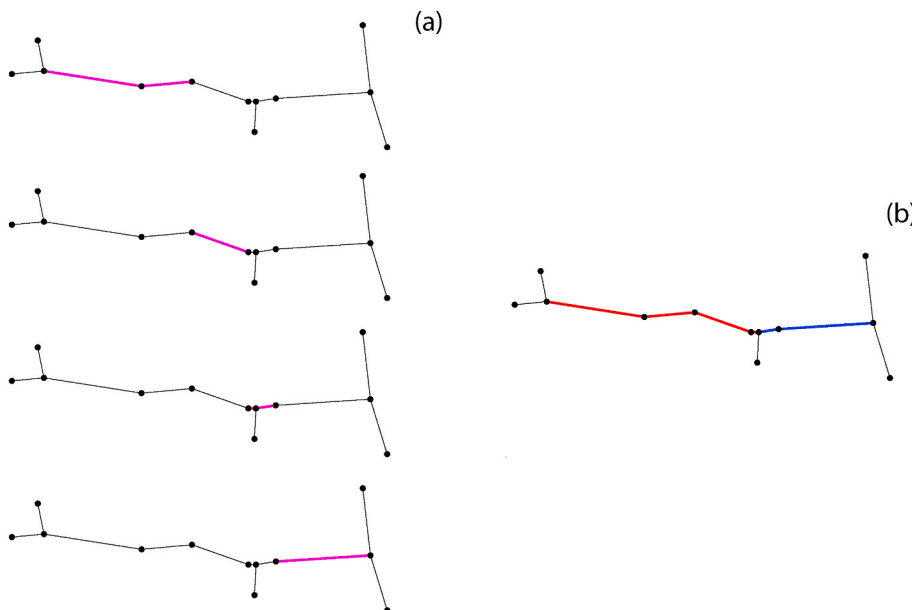


**Fig. 9.** Resolving artificial fragmentation (a) an example of an artificially segmented fracture is shown which is saved as four polyline entries within the shapefile. These are highlighted in magenta. The first segment (top) is of topology type Y-V-V (where V used to denote a degree-2 node and Y a degree-3 node), second is a V-V segment, third is a V-Y-V segment, and the last one at the bottom is a V-Y segment. (b) The graph edge linking converts the fragmented four segments into two segments which are both of Y-Y topology type. The routine does both merge and split operations to ensure that there are no attribute table entries in the shapefile that begin or terminate in degree-2 nodes.

connected to the start and terminating nodes of each step-out are identified. A walk is identified for each of these edges. Though the step-out is a geometric feature that impedes the possibility of a walk, there are still possibilities of walks looking upstream on both directions away from the step-out. A decision is made as to which direction alongside the step-out provides the best increase in walkability based on length of

walk. Once this is identified, the node of the step-out that causes the bottleneck is moved to a more preferable alignment. The sequence of graph manipulations involved in this flattening operation consists of adding three edges, removing three edges, adding a node, and removing one node. The step-out flattening procedure therefore improves the walkability in one direction.

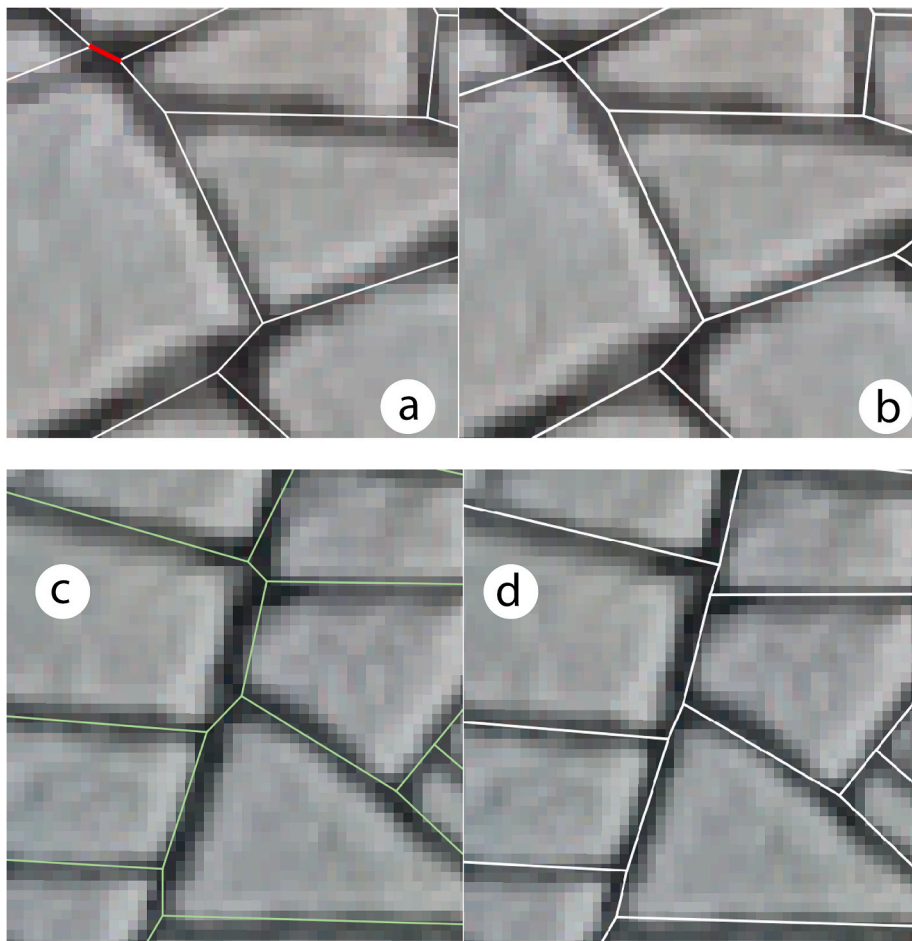


**Fig. 10.** An example of automatically resolving a stepout by a merge operation (a) stepout Y-Y segment depicted in red (b) Y-Y segment removed and edges merged to form an X node. An example of automatically resolving a stepout by a flatten operation from Area 4 (c) stepout segments with varying strike that can cause loss in continuity when parsing for possible walks (d) stepout segments flattened. (For interpretation of the references to colour in this figure legend, the reader is referred to the Web version of this article.)

#### 4.4.4. Straightening fracture segments

During piecewise polyline fitting as performed when vectorizing fracture traces (see Fig. 11(a)), a large number of points are inserted to represent the natural sinuosity of fracture traces. Within the graph representation these points are degree-2 nodes and are the predominant topology type. Although these nodes provide useful local information, in terms of overall macro-network topology, it may be useful to *straighten* or *flatten* the graph edges by removing these degree-2 nodes and replacing them by single edges between the non-degree 2 nodes. This type of graph manipulation involves removal of all edges that either start or end in degree-2 nodes (or both) and addition of single edges between the non-degree 2 nodes. The implementation of this function is attached in the

supplementary code. The effect of such an edge straightening operation is depicted in Fig. 11(b).

#### 4.4.5. From fracture traces to geologically significant fractures

The geological identification of a fracture in the outcrop or from image data is that of a discontinuity feature that is geometrically continuous with the tip extremities either abutting another fracture, cutting across another fracture, or terminating within rock matrix. In a typical manual interpretation using UAV-derived imagery, the interpreter draws polylines in a digitizing software (eg. Adobe Illustrator, Coreldraw, QGIS, ArcGIS etc) tracing across image pixels that seemingly correspond to a perceived fracture using visual cues within the image

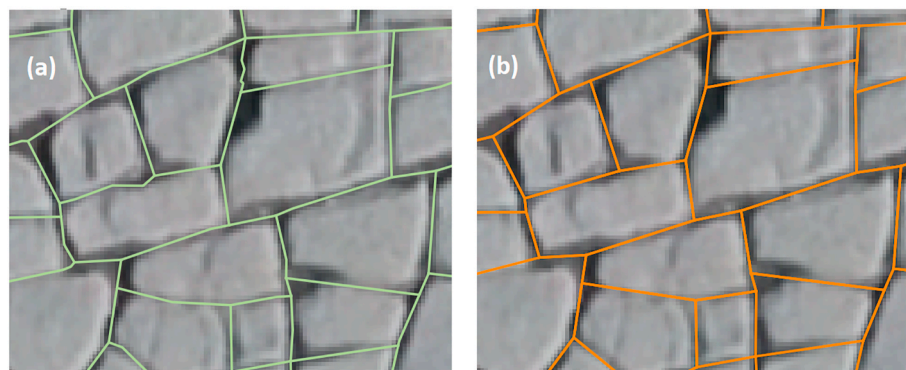


**Fig. 11.** An example of straightening of fracture segments (a) original fracture network with piece-wise linear segments and degree-2 nodes (b) fracture segments which are straightened removing the degree-2 nodes.

coupled with specific knowledge of the particular outcrop and general training in structural geology. There are many ways in which such a GIS-derived interpretation may be biased and lacking repeatability as discussed in Andrews et al. (2019) and Peacock et al. (2019). Given these considerations, it is useful to have an automated method of obtaining geologically significant fractures (or fracture sets) rather than just fracture segments. A simple way to assign segments to individual sets is to sort based on striking angles as is done in popular tools such as FracPaQ (Healy et al., 2017), and NetworkGT (Nyberg et al., 2018); however, this may be difficult when fractures are very sinuous. Additionally as pointed out by Peacock et al. (2018) and Andrews et al. (2020), orientation sets need not always equate to an age sets and there are drawbacks involved in only considering strike.

The graph representation of a fracture network is complete when we have list of nodes, spatial positioning data corresponding to each node, a list of edges with start and terminating points indexed as per node numberings, and a list of edge sequences to represent each fracture. Automatic tracing cannot yield the edge sequences so that they represent sets of fractures (tip-to-tip). To this end, a function is developed to automatically identify continuous paths along graph edges based on twin rules of connectedness and small strike variation. The routine considers each edge individually and checks if adjacent edges fall within the threshold of edge strike, on either ends of the edge. Sequences of edges (or walks) are assigned as fractures. The routine is attached in the supplementary code. An example of a continuous and sinuous fracture automatically combined from graph segments are shown in Fig. 12.

In a related publication based on the same dataset as ours, Passchier et al. (2021) manually interpret and classify continuous edges as belonging to a single generation. We have compared the results of the automated function described in this section to the manually assigned joint generations of Passchier et al. (2021) and there is generally a good agreement.

#### 4.4.6. Computing dual graphs

A dual graph can be computed from a primal graph if the edges sequences corresponding to individual fractures (tip-to-tip) are known or is computed using function described in Section.4.4.5. The dual graph depicted in Fig. 2(b), was computed from a shapefile in which fracture id's of manually interpreted fractures were already been listed. Given the edge sequence information, obtained either from manual interpretation or automatically, the procedure to compute the dual is by initializing an adjacency matrix whose size is equal to number of fractures ( $A_{adj}$  is an  $n \times n$  matrix where 'n' is the number of tip-to-tip fractures). By parsing through the intersections made by each fracture with others, the sparse adjacency matrix is then built up by filling in rows and



Fig. 12. Continuous and sinuous fracture from Area 4 automatically joined from graph segments with a strike threshold of 20°. Note that the strike of the start and end segment of the fracture vary by more than 50°.

columns corresponding to fracture intersection. The function that accomplishes this is included in the supplementary code.

## 5. Results

The methods in Section.4 are applied to image tiles corresponding to the five selected areas and based on these we generate five large networks. The created fracture data are in the form of spatial graphs and shapefiles attached in the supplementary data. A summary of the number of nodes, edges, and tip-to-tip fractures (or walks) for each area is tabulated in Table 2. Edge/node and edge/walk ratios are also shown as they give an indication as to the connectedness of the networks. In order to illustrate the level of detail within the generated network data, zoomed cut-out regions from Area 2 (see Fig. 13(a)-13(c)) and Area 4 (see Fig. 13(e)-13(f)) are depicted. From the cut-outs of Area 2 in Fig. 13(a)-13(c), there are clear visual differences in fracturing even though the orientations of fractures are quite consistent among all three samplings. This is however, not the case in the cut-outs from Area 4 shown in Fig. 13(d)-13(f). In Fig. 13(e), a radial NW-SE trending fracture pattern that is orthogonally cut by NE-SW fractures can be observed. The fracturing style is very different in Fig. 13(d) with no radial fracturing, higher fracture intensity, and smaller bounded blocks. In Fig. 13(f), the fracturing intensity is highest with even smaller bounded blocks.

### 5.1. Length distributions and fracture set directions

Trace length distributions corresponding to the five areas are depicted in Fig. 14. Trace length distributions show the lengths from fracture tip-to-tip. These are affected by boundaries of the sampled regions which may be observed by comparing the plots of largest areas, 2 and 4, with the other three. In Fig. 15(a) and Fig. 15(b) we depict fractures plotted by their length classified into three logarithmic bins for Areas 1 & 3 which are stratigraphically the same layer. Similarly, the length-binned fractures are depicted for Areas 2, 4 & 5 in Fig. 15(c), (d), and Fig. 15(e) respectively.

The rose plots depicted in Fig. 14 are computed from strike data that is a length-weighted average of the strike of edges that sum up to a tip-to-tip fracture. The rose plots highlight differences in fracture orientation between the layers. Orientation of the fractures do not vary significantly in Areas 1 & 3. However, Areas 2 & 4 from the same stratigraphic layer have considerably different fracture orientations. This is illustrated in Fig. 15(d) with Area 4 containing curved and radial fractures. However, Area 2 does not have any curved fractures (see Fig. 15(c)). Similar to Area 4, Area 5 also has curved fractures as can be seen in Fig. 15(e). The scatter in rose-plots corresponding to Areas 4 & 5 is related to the presence of the curved joints.

From Fig. 15(c), (d), and Fig. 15(e), spatial variations in the distribution of fractures in Areas 2, 4, and 5 can be observed. The longest joints in Area 2 display a spatial variation with a larger concentration to the SW (see Fig. 15(c)). In case of Area 4, the radial and curved fractures which are also the longest are located in the western part of Area 4 (see Fig. 15(d)). The occurrence of these long, radial joints diminishes to the east of Area 4. In the case of Area 5, the long fractures has strikingly different curvature directions towards its east compared to its west (see Fig. 15(e)).

Table 2  
Summary of primal graph structure.

Region	Edges (e)	Nodes (n)	e/n	Walks (w)	e/w	Polygons
Area 1	42301	30299	1.39	18078	2.34	11992
Area 2	364703	228661	1.59	123592	2.95	136053
Area 3	40243	26372	1.52	16900	2.38	13874
Area 4	365333	235089	1.55	141344	2.58	129690
Area 5	78151	49771	1.57	28892	2.7	27220

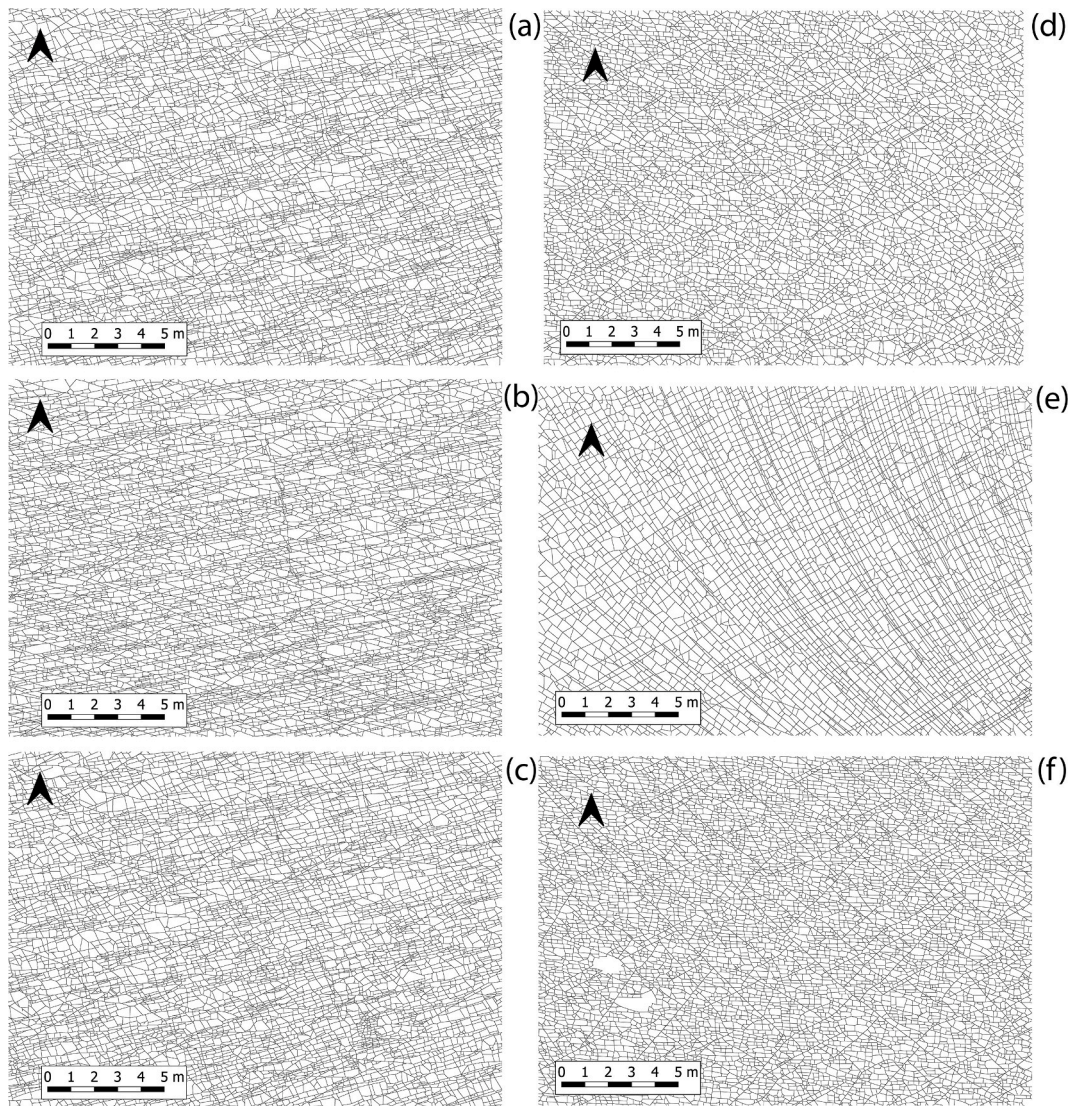


Fig. 13. Samples of fracture networks from a single stratigraphic layer across Area 2 and 4 highlighting the differences in fracture network organization. Samples (a), (b), and (c) are from Area 2 and (d), (e), and (f) are from Area 4.

### 5.2. Network topological summary

From Manzocchi (2002), Sanderson and Nixon (2015), and others, an I-node corresponds to a fracture tip that is isolated, a Y-node is analogous to fracture tip that has abutting interactions with other fractures (or splaying fractures), and an X-node represents an intersection where one fracture crosses another fracture. The proportions of each node type can be summarized in an I-Y-X ternary diagram. To quantify network topology, we use node degree histograms instead of I-Y-X ternary plots. This is because of the need to depict node degrees greater than four which are not unusual in large-scale networks as is observed in the Lilstock pavement. Additionally, in the case of dual graph representations, where fractures are represented as nodes, the node degree can be larger (Valentini et al., 2007a). The node degree distribution of the primal graphs corresponding to the five networks is depicted in Fig. 16. The node degree distribution of the dual graphs corresponding to the five networks is depicted in Fig. 17(a)–(e). Degree distributions of all the primal graphs indicate that the predominant node topology are Y-nodes with a 70–80% contribution followed by X-nodes. A summary of primal graph edge types based on topology is shown in Table 3.

The dual graph degree distributions provide insight into the

connectivity behaviour of each network. The topological summary of the dual graphs are tabulated in Table 4. The node degree value indicates the number of connections that a fracture makes with other fractures within a network. Maximum node degrees in dual graphs are observed from Areas 4 and 5 which contain continuous and long, radial fractures. The correlation between dual graph degree (number of intersections made a fracture) and the fracture length is also plotted in Fig. 17(f)–(j) depicting a positive correlation between fracture length and number of intersections. The number of connections is least in Areas 1 and 3. This is possibly an effect of sample size as these regions are the smallest and their spatial extent in the N-W direction is quite thin. Area 2, despite covering more area than Area 5, has a lesser maximum dual degree.

### 5.3. Bounded area distribution

The fracture patterns develop and enclose bounded regions of unfractured rocks. These enclosed polygonal areas are extracted from the spatial graphs by identifying the primary cycles that are created by edges. The spatial distribution of areas corresponding to these polygonal regions is depicted in Fig. 18 as a choropleth and depicts the variation across the layers. Histograms of the area distributions of each layer is

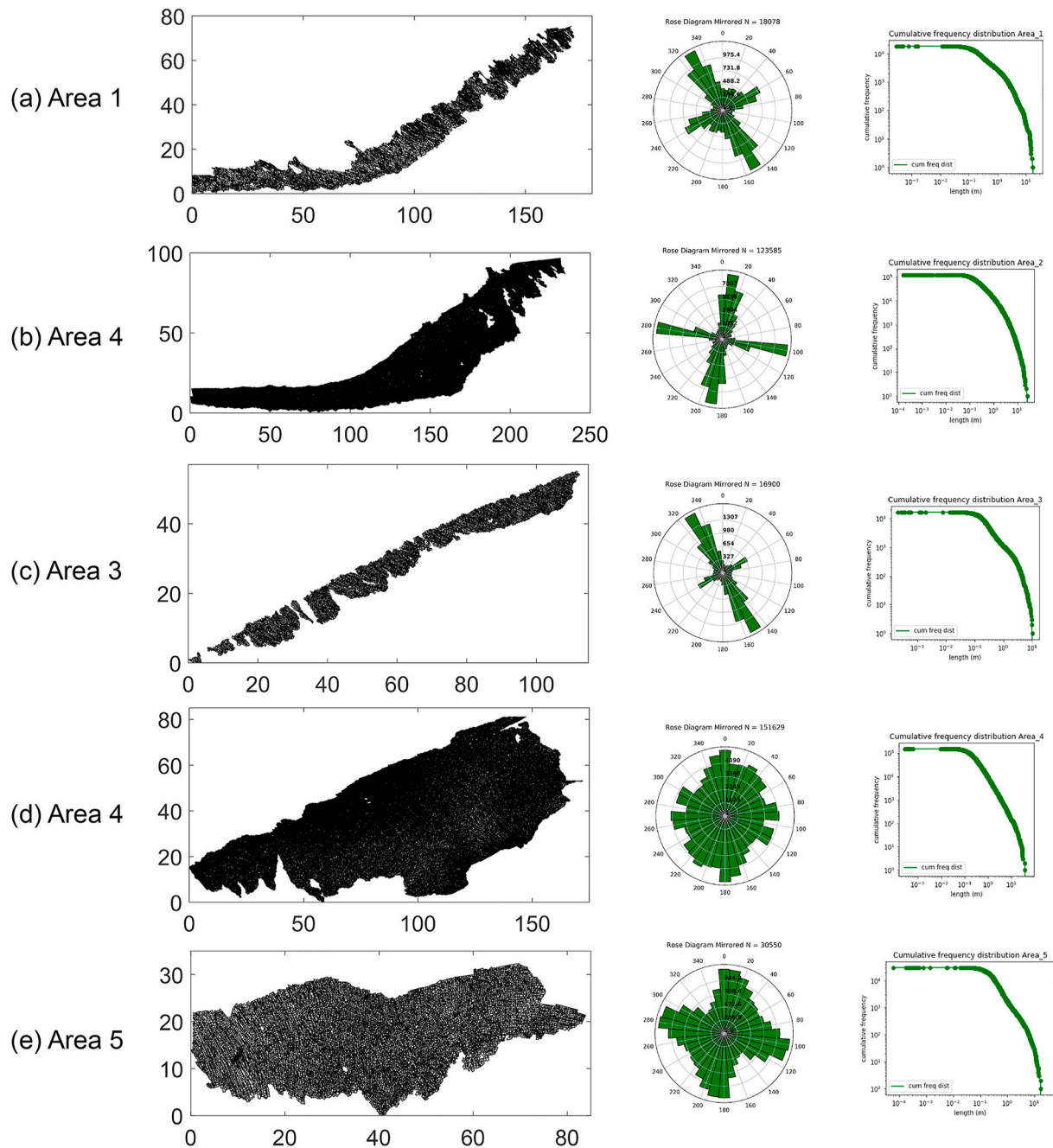


Fig. 14. Fracture network trace maps for all areas with corresponding rose plots and cumulative trace length distributions (a) Area 1 (b) Area 2 (c) Area 3 (d) Area 4 (e) Area 5.

depicted in Fig. 19. Area 1 appears to have the largest block areas, followed by similar distributions for Areas 3 and 5. The largest Areas 2 and 4 have smaller block areas with visibly more intensive fracturing.

5.4. Spatial  $P_{20}$  and  $P_{21}$

Fracture persistence measures ( $P_{ij}$ ) formulated by Dershowitz and Herda (1992) are used to investigate the spatial differences in fracturing. The fracture intensity,  $P_{21}$  and fracture density  $P_{20}$  metrics are computed using the box-counting method by overlaying the networks with a cartesian grid of box size of  $2.5 \times 2.5m$ . Fracture intensity ( $m/m^2$ ) involves computing 2D trace length per area for each grid box. This is depicted for all areas in Fig. 20(a). Fracture density ( $m^{-2}$ ) computes the number of segments within each grid box and this is depicted in Fig. 20(b). The

persistence results reveals regions within the outcrop with different fracturing motifs. Area 1 has the least fracturing intensity and density which is uniform in the spatial distribution. Area 3 also is homogenous in the type of networks present. The greatest variation is in Area 4 which has clear regions of low and high  $P_{21}$  and  $P_{20}$  with a demarcable boundary. Area 2 has the most intense fracturing over all regions is in the eastern parts of Area 2. Similar intense fracturing regions can also be seen in the northern parts of Area 4. These are not fracture corridors but progressively intense fracturing with smaller block areas.

6. Discussion

Manually tracing fracture networks from image data is time-consuming and can introduce various types of biases depending upon

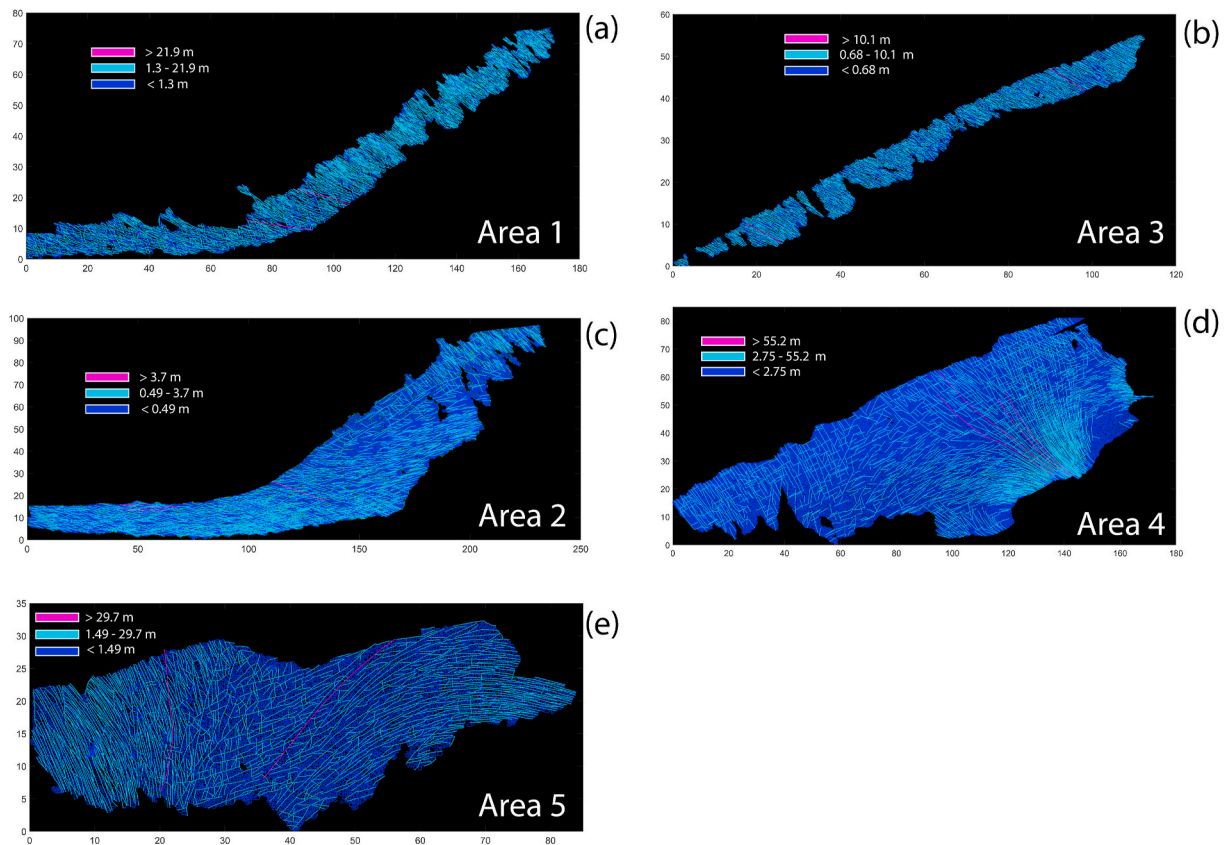


Fig. 15. Plotting fractures by logarithmically spaced length bins (a) Area 1 (b) Area 3 (c) Area 2 (d) Area 4 (e) Area 5.

skill, style, and perseverance of the interpreter. These challenges are evident from the observed networks in the structural geology literature which are not large and not continuous enough to study spatial network heterogeneity or do not have sufficient resolution to correctly identify topology. Automatic tracing affords rapid and reproducible network results which can be applied to large image datasets. In case of the Lilstock pavement, high image resolution, enlarged apertures due to erosion, high contrast in imagery between the wet apertures and dry surface, and lack of vegetation, aided in easily applying automatic mapping. One major drawback associated with automatic interpretations which precludes direct usability by a structural geologist and which were evident from the results of Prabhakaran (2019) is that the detected segments were not yet organized into geologically meaningful, tip-to-tip fractures.

The treatment of fracture networks as graph data structures with spatial positioning allows us to perform various sequences of graph manipulations to rectify these issues and convert the data into geologically realistic fractures. The combined use of automatic tracing and application of such specific routines have resulted in a spectacular, large-scale fracture network dataset with unprecedented spatial coverage and resolution. The network data is of great relevance as it can be used to obtain valuable insights into spatial arrangements of fracture networks and network morphogenesis. In this section, we delve into possible reasons for the observed spatial variations in network geomorphology. Issues regarding the applicability of automatic mapping and how large-scale network data can be leveraged are also considered.

### 6.1. Spatial heterogeneity

One of the interesting results of our fracture maps is the lateral differences in patterns. Areas 1 and 3 have relatively less spatial variation as can be quantified from spatial plots of fracturing intensity,

density, and polygonal areas (see Fig. 20(a) and (b), Fig. 18). They are also the smallest regions with long and thin strips of exposed rock. Area 1 corresponds to regions with the least fracture intensity and density, and highest bounded areas. The most spatially extensive layer, comprising of Area 2 and 4 depict the most striking variations. From previous work by Gillespie et al. (2011); Rawnsley et al. (1998); Hancock and Engelder (1989) and many others, the long radial, fan-like fracture sets are hydraulically-driven and originate from stress concentrations on the small fault. This region in the SE of Area 4 also has the least fracturing intensity with wide spacing between the radial fractures. The interference of small low-displacement faults can also be seen in the NE region of Area 2 which again has a low-fracture intensity. Similar to Area 4, Area 5 also contains highly sinuous fractures that can be linked to the NE trending regional fault. In Area 5, the long, radial fractures have strikingly different curvature directions towards its east as compared to its west (see Fig. 15(e)). These effects totally disappear in Areas 1, 2, and 3 which have mostly straight fractures. Within Area 2, a trend of high fracturing intensity can be observed towards the SW which progressively decreases towards the NE. Area 5 has the largest fracturing intensity in its centre and this progressively decreases to its east-west peripheries. Passchier et al. (2021) highlighted spatial variations in the presence of joints in the regions covered by Areas 2 and 4. From a total of eight identified jointing generations, only two are distributed evenly across both areas. Three sets of joints exclusively appear in Area 2 but are absent in Area 4. Another three sets are found in both Areas 2 and 4, but they are restricted to certain localized regions. The spatial variation of the polygonal area distributions (Fig. 18) follows a similar trend as the fracture persistence plots (Fig. 20(a) and (b)). The spatial variation in block areas is likely to depend upon the thickness variation of limestone and underlying shale layers (Belayneh and Cosgrove, 2004).

The reasons behind spatial variation may also originate from factors not observable from simple photogrammetric data. For example,

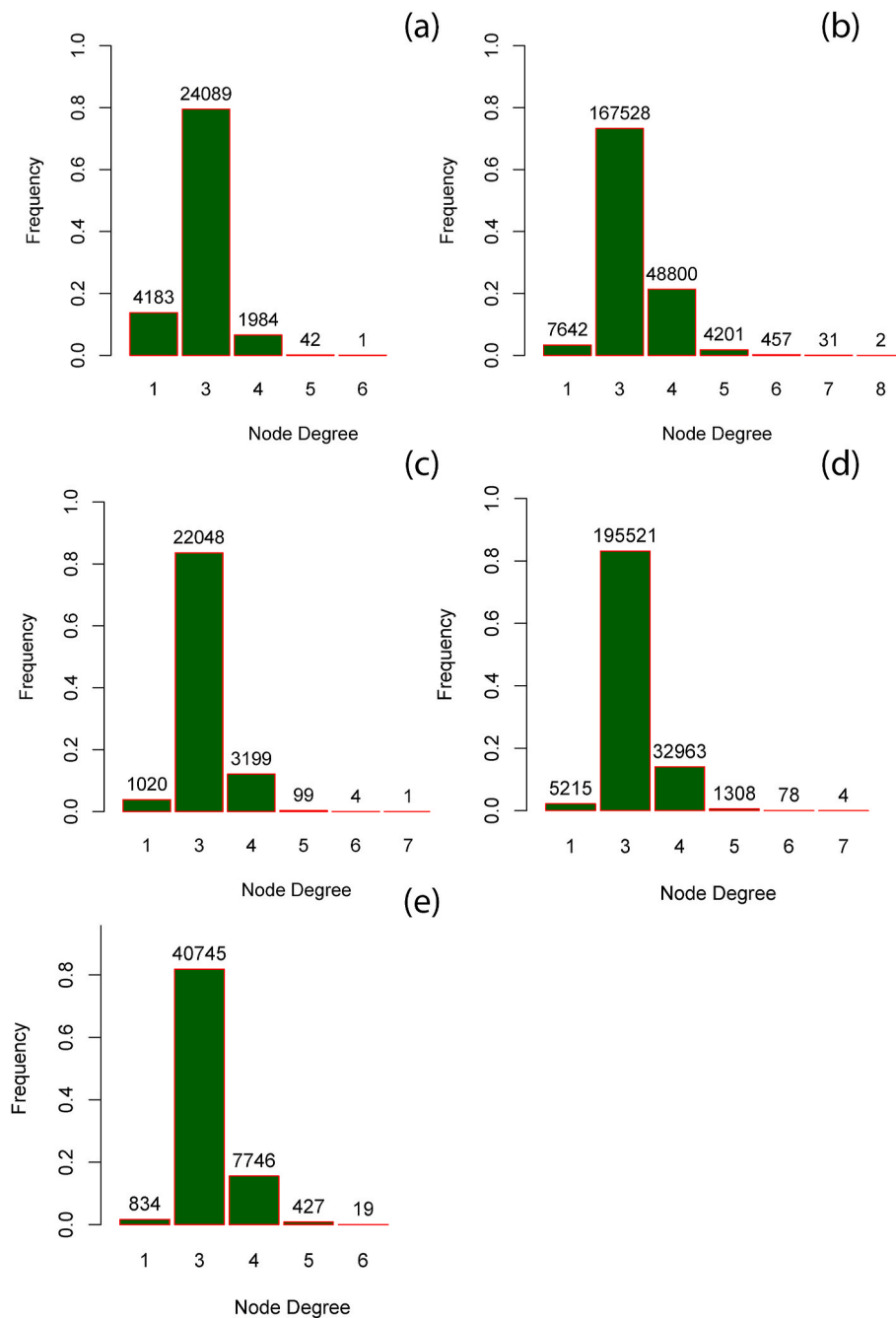
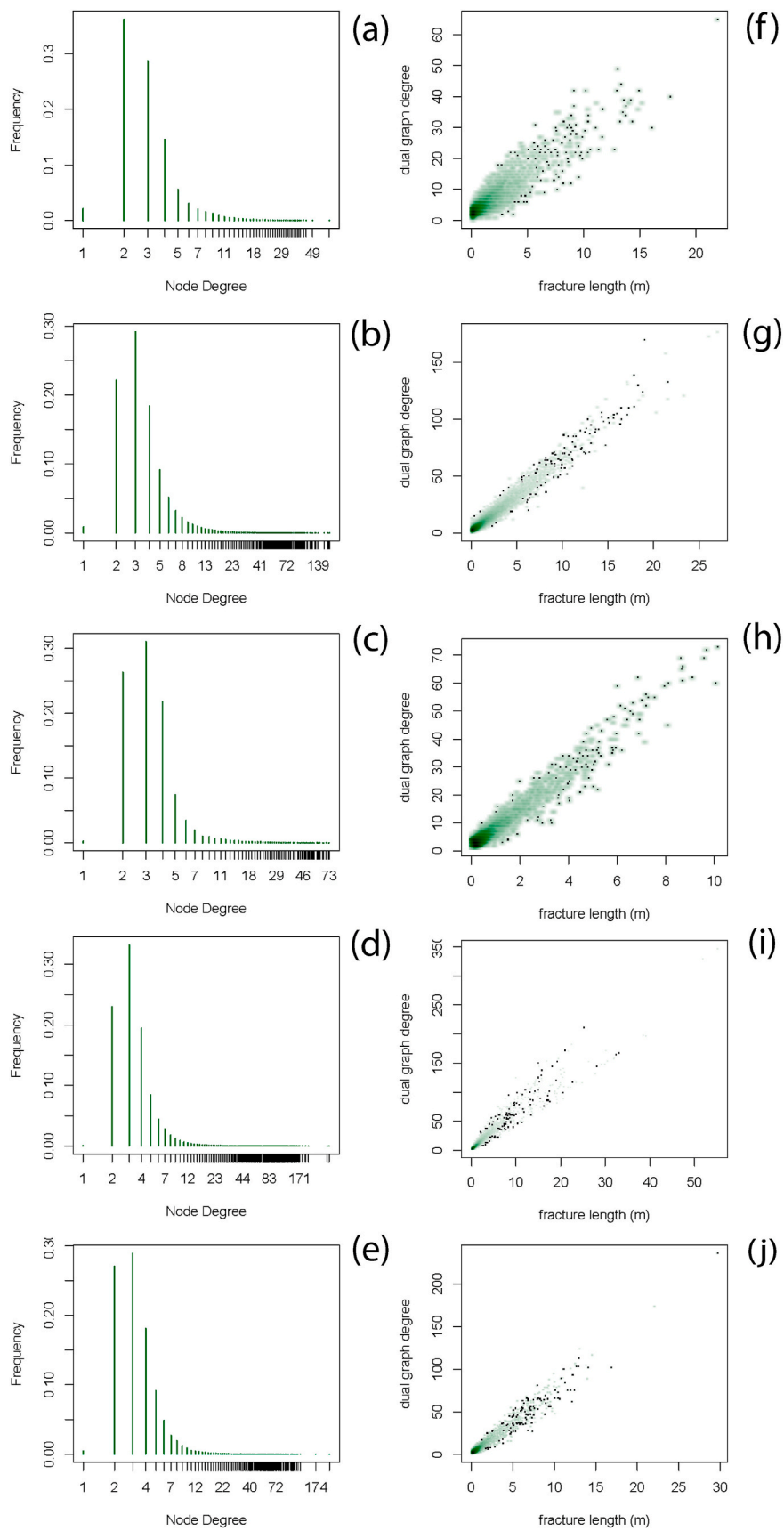


Fig. 16. Degree Distributions for the primal graphs with number of nodes corresponding to each topology type (a) Area 1 (b) Area 2 (c) Area 3 (d) Area 4 (e) Area 5.

differences in fracturing may emanate from local variations in layer thickness, due to changes in mineralogical composition of the host-rock, and orientation/strengths of pre-existing structures. Our image resolution does not include vein or stylolite networks which are also present in the outcrop and whose spatial variation may have an influence on the development and of the barren fracture networks that we have mapped. Spatial layer thickness can be estimated by methods such as ground penetrating radar (GPR) and mineralogical variation can be explored using UAV-based sensors such as magnetic and hyperspectral imaging. Therefore, it is suggested that further investigations into spatial variation in fracture networks should incorporate data fusion from a variety of UAV-mounted sensors, coupled with field-level and ground truthing of features that are below remote sensing spatial resolutions.

### 6.2. From traces to timing

Previous work on the Bristol Channel summarized in Section.3 have focussed on relationship between structural history of the region, exposed fractures, and other large deformation features. Identifying fracture generations and sequences of network evolution is routinely done based on geometric criteria and topological relationships of fracture tips, sometimes supported by geochemical analysis of cement within fractures. The problem of identifying fracture timing from the automatically traced fractures was not in the scope of this contribution. Using the same dataset as we have used, [Passchier et al. \(2021\)](#) identified eight generations of fractures traced segments without resorting to a fully detailed network interpretation. The oldest generations were considered to be the most continuous and longest which do not abut against others. Subsequent generations were then identified based on



**Fig. 17.** Degree Distributions for the dual graphs (a) Area 1 (b) Area 2 (c) Area 3 (d) Area 4 (e) Area 5. Correlation between dual Degree and trace length (f) Area 1 (g) Area 2 (h) Area 3 (i) Area 4 (j) Area 5.



**Table 3**  
Summary of primal graph edges based on topology.

Edge type	Area 1	Area 2	Area 3	Area 4	Area 5
1-1		4			
1-3	4041	7048	1007	5127	783
1-4	139	552	12	87	43
1-5	3	27	1		8
1-6		7		1	
3-3	30612	176360	27186	238130	47983
3-4	6815	127218	10355	99922	23793
3-5	182	13740	386	4902	1610
3-6	5	1708	18	329	83
3-7		141	6	23	
3-8		9			
4-4	478	30074	1161	15094	3327
4-5	25	6328	100	1522	465
4-6	1	884	6	129	29
4-7		63	1	4	
4-8		7			
5-5		392	4	53	25
5-6		115		9	2
5-7		11		1	
6-6		13			
6-7		2			
Total	42301	364703	40243	365333	78151

**Table 4**  
Summary of dual graph structure.

Region	Nodes (n)	Edges(e)	e/n	Max degree
Area 1	18078	34077	1.88	65
Area 2	124006	301077	2.42	177
Area 3	16900	36320	2.14	73
Area 4	141344	314537	5.27	347
Area 5	28892	65867	2.28	236

strike and abutting criteria w.r.t each older joints generation. In their study, a correlation between length and age seemed probable with only few exceptions. In the same work, there are also highlighted cases where sequential rule-based joint identification results in *Escherian* paradoxes.

Another study by Wyller (2019) focussed on an area that roughly conforms to the western parts of Area 4 and was able to identify ten sets of joints using statistical analysis of joint lengths, orientations, and topology. In this study as well, assigning hierarchies based on abutting relations result in paradoxes which Procter and Sanderson (2018) and Wyller (2019) refer to as *backcycling* between joint generations.

The above studies are based on the assumption that abutting and cross-cutting relationships are a sufficient criteria, if not necessary, to be able to delineate fracture sets into a hierarchy of fracturing episodes. Such approaches may not always suffice, for instance, if fracturing drivers are due to high-deformation episodes or if there is evidence of complex structural inheritance. In outcrops such as the Lilstock pavement, where fractures are mostly formed in low-deformation settings, simple geometric criteria as proposed by Passchier et al. (2021) may be programmed to automatically assign fractures into hierarchical episodes. Given large networks and well-defined criteria, it might be more prudent to use statistical strategies such as Markov chains to automatically assign generations (Snyder and Waldron, 2018). The combinatorial approach of Potts and Reddy (2000) in the form of younging tables to identify deformation histories may also be applied in an automated manner. In future work, such automated approaches may be applied to the full-detailed fracture networks presented in this paper to compare automatically-assigned generations to those that have been manually-assigned in previous literature relevant to the Lilstock pavement.

6.3. Extent of applicability of automatic methods

We have been able to extract a very large number of geologically relevant fracture traces focussing only on the opening-mode fractures that are visible from a flying altitude of 20–25 m. The quality of the interpretations are comparable to the work of a manual interpreter and

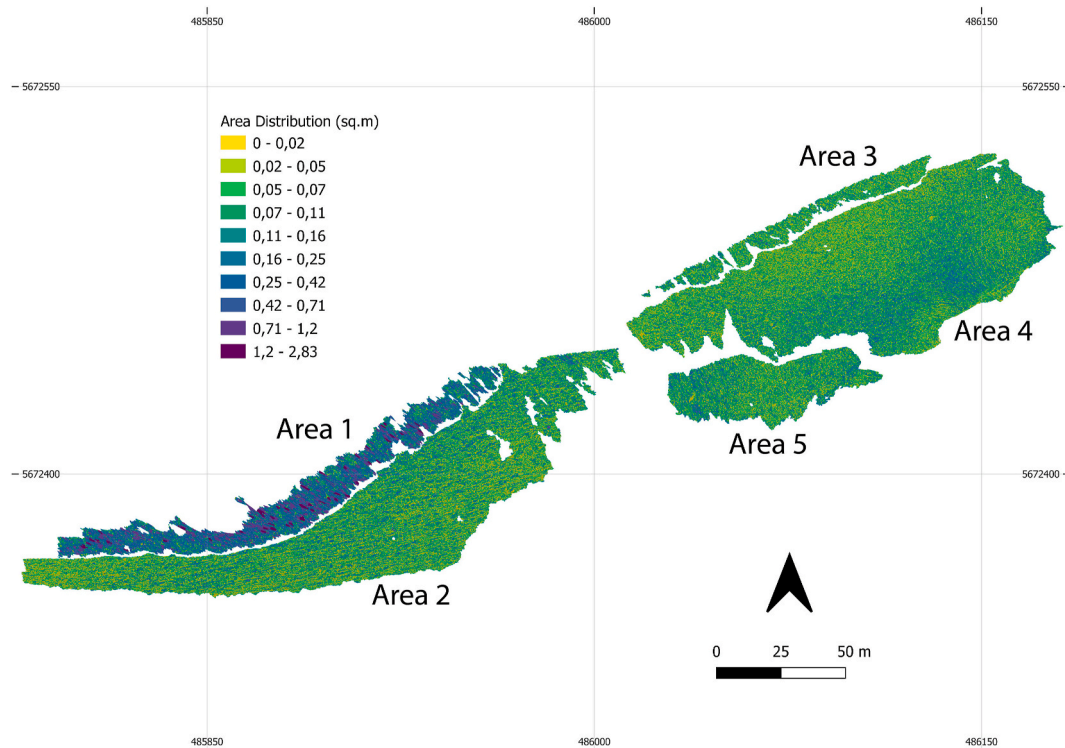


**Fig. 18.** Spatial distribution of polygonal regions highlighting the variation in fracturing across different areas.

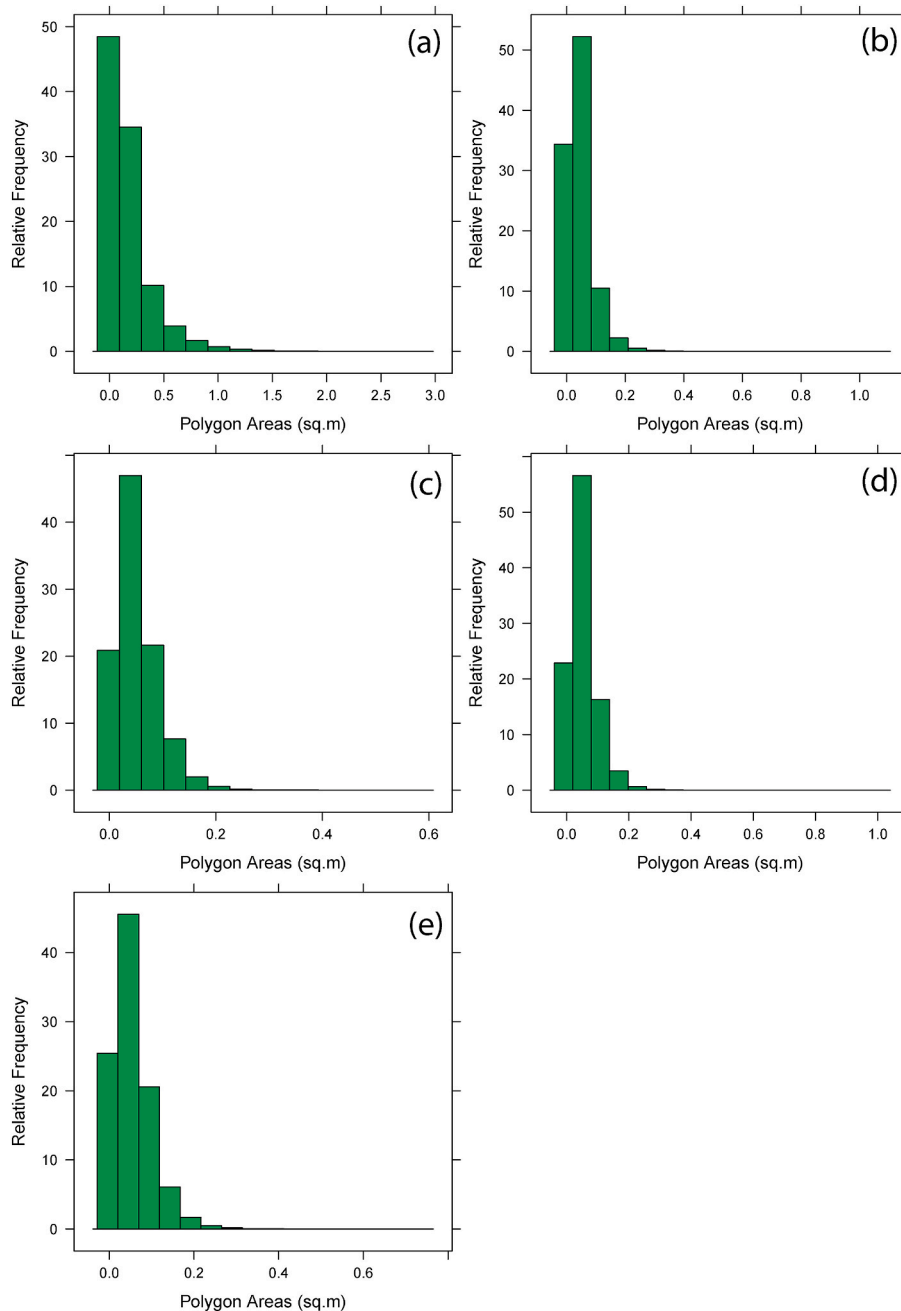


Fig. 19. Bounded area distributions with relative frequency in percentages (a) Area 1 (b) Area 2 (c) Area 3 (d) Area 4 (e) Area 5.

this is attained in much less time (Weismüller et al., 2020a,b). Often, the error in automatic tracing results are within the limits of subjectivity associated with even a well-trained interpreter. The largest variation in interpretation between manual and automatic is the creation of stepped-out segments. This is due to the fact that unlike manual interpretation where the interpreter can make a decision on a possible fracture intersection considering the full outcrop image, automatic methods make use of local information in the image which leads to uncertainty in regions which are more eroded than normal. The presence of step-outs sections was observed by Weismüller et al. (2020a,b) when comparing topological differences between the two approaches and revealed that manual interpretations result in topological distributions skewed to higher node degrees. From a network connectivity point-of-view, such a configuration may be correct but this can result in shorter length distributions. Despite the fact that multiple interpreters may differ in the choice of a fracture tip start and end (as shown by Andrews et al., 2019

in experiments with multiple participants), the issue of curtailed length distributions are less likely to arise in manual tracing as interpreters use multiple global cues available within an image to decide the continuity of a trace. We addressed these issues using the step-out fixing functions. The methods developed here are extendable to other photogrammetric datasets.

#### 6.4. Extension of outcrop fracture network data

In subsurface applications, geomodelers often have to contend with sparse borehole fracture data as the only available ground-truth. Since geophysical imaging resolution are often too coarse to resolve subsurface fractures, outcropping fractures have long been considered as analogues to guide subsurface discrete fracture network models. In a typical subsurface situation, it is required to be able to extrapolate away and interpolate between points of well control where fracture data exists

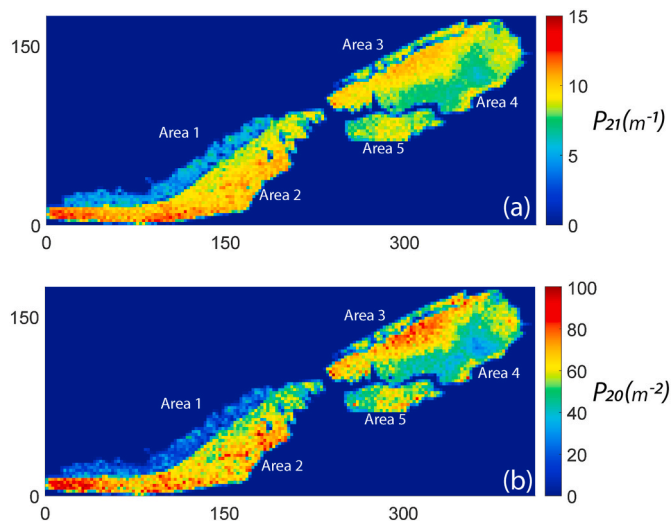


**Fig. 20.** Fracture intensity,  $P_{21}$  ( $m/m^2$ ) for all areas (b) Fracture density,  $P_{20}$  ( $m^{-2}$ ) for all areas.

in the form of cores, formation micro-images (FMI), and resistive/acoustic logging. This is a highly ill-posed problem as the naturally heterogeneous behaviour of fracture patterns are typically under-represented. This is due to inherent sampling bias within each well data point and well as uncertainty in relationship between large-scale geological drivers.

The commonly used methods for subsurface fracture network modelling are based on stochastic point processes that use 1D well data input such as fracture size, type, intensity, number of sets, and cumulative length distributions (Thovert et al., 2017). Stochastically-generated DFNs that utilize such sparse data to extrapolate, are often limited in their ability to represent fracture clustering effects, spatial variations in fracture orientation, and topological connections, all of which are observable in natural fracture networks.

Alternative methods to stochastic point-process based methods such as the semi-variogram approach of Hanke et al. (2018) applied to areal fracture intensity and fracture intersection density maps, and the multipoint statistics approach of (Bruna et al., 2019a,b) which use training images of user-defined outcrops can help in incorporating more geologically-realistic fracture networks into geological models.

In this respect, one needs to assess the fracture network properties that are to be replicated and for which 2D fracture trace maps can provide additional value. From our analysis of the large-scale Lilstock fracture networks, we would suggest that DFN generating methods should also be able to replicate bounded area distributions. This may be justified by the fact that fracture networks influence effective rock permeability also through time-dependent diffusive effects from the matrix. Since matrix block area distributions contributes to the matrix-fracture fluid exchange, it needs to be represented as a parameter. A second useful parameter that arises from 2D trace maps is the correlation between fracture length and number of intersections. From our analysis of dual graphs (Fig. 17), we find this to be positively-correlated.

In the work of Andresen et al. (2013) and Vevatne et al. (2014) where fractures are represented using dual graphs, the networks display the property of *disassortativity* in which nodes of larger degree (longer fractures) share coordination with nodes of a smaller degree. This is also referred to as *small-world behaviour* (Watts and Strogatz, 1998), a property shared by many other classes of networks. A DFN generating technique must also be able to replicate disassortativity in network realizations.

At this juncture, we revisit the point on applicability of outcrop-derived fracture networks. Recent work by Laubach et al. (2019) have raised questions on the use of fracture network data that has no provable

correlation to subsurface fractures. Ukar et al. (2019) and Laubach et al. (2019) proposed protocols to identify suitable analogues based on mineral-lining evidence in fractures. In the case of network data presented in this article, we repeat this caveat that though the data is useful in studying the fracture network properties and their spatial distribution, caution needs to be exerted when extrapolating to subsurface conditions.

Although the results presented in this contribution have a very clear network structure with a very low proportion of I-nodes, many outcrop fracture studies and subsurface data indicate the prevalence of sub-parallel fractures where the isolated type of topology is the most common. Some examples of such systems are documented by Odling (1997), National Research Council (1996), Wüstefeld (2010) etc. Such fractured systems which have poor connectivity among the fractures still have an impact on fluid flow behaviour (Philip et al., 2005), and there is a need for large-scale data pertaining to such systems.

## 7. Conclusion

We present automatically extracted, large-scale fracture networks from limestone pavements the Bristol Channel, UK using photogrammetric data previously published by Weismüller et al. (2020a,b). The automatic extraction process combines methods from Prabhakaran et al. (2019) and a series of programmatic routines introduced in this contribution. The functions developed receive fracture network input in the form of a graph data structure, perform node/edge manipulations on the graph so as to rectify issues such as lack of connectivity, artificial segmentation, and linking of segments. The resultant graphs can then be converted into geologically significant fracture traces amenable for further analysis. In summary, the main findings of this contribution are listed below.

- Fracture networks from five fractured limestone pavements spread over approximately 17,000 sq.m are automatically extracted using the complex shearlet transform method from UAV-borne photogrammetric imagery. From a spatial graph perspective, the number of fracture segments or edges is nearly 800,000.
- A set of programmatic functions is designed to perform topological manipulations on fracture segments, resolve discontinuities, resolve artificial fragmentation, and combine segments into geologically significant fractures. The programmatic routines are applied to the automatically extracted fracture segments and a large-scale fracture dataset comprising around 350,000 fractures is presented.
- Length distributions of fracture networks corresponding to the five regions follow a power-law scaling. Fracture orientations in two regions show considerable scatter owing to presence of sinuous fractures, while fractures in the other three regions are organized into well-defined orientation clusters.
- Analysis of node degree distributions of primal graphs indicate that the most common topology type is the degree-3 node or Y-node indicating the probable sequential development of the networks in each of the five studied outcrops with younger and shorter fractures abutting on to older and longer fractures.
- In all the mapped areas, degree distributions of dual graphs positively correlate to the total fracture lengths highlighting the fact that longest fractures are likely to have the largest topological length. All the five networks display this property of disassortativity where fractures possessing smaller degree attach on to fractures possessing a higher degree.
- The networks possess both inter-network and intra-network variability despite belonging to similar stratigraphic layers and in weakly deformed settings. The variation is quantified using spatial maps of block area distributions, fracture density, and fracture intensity, and reveal that fracturing patterns in the Lilstock pavement are heterogeneous over distances of tens of metres.

## CRedit authorship contribution statement

**Rahul Prabhakaran:** Writing – original draft, Conceptualization, Methodology, Software. **J.L. Urai:** Supervision, Writing – review & editing, Data curation. **G. Bertotti:** Supervision, Conceptualization, Writing – review & editing, Resources. **C. Weismüller:** Data curation, Writing – review & editing. **D.M.J. Smeulders:** Funding acquisition, Project administration.

## Declaration of competing interest

The authors declare that they have no known competing financial interests or personal relationships that could have appeared to influence the work reported in this paper.

## Acknowledgements

We would like to thank Quinten Boersma (TU Delft) for his assistance with Digifract python scripts which were applied in generating some plots in this article. Martijn Passchier (RWTH Aachen) is thanked for sharing his manual interpretations and fracture generations in the Lilstock outcrop.

## Appendix A. Supplementary data

Supplementary data to this article can be found online at <https://doi.org/10.1016/j.jsg.2021.104405>.

## Code availability

1. The code used for automatic fracture detection is published as supplement to Prabhakaran (2019) and is available to download from the following GitHub repository: <https://github.com/rahulprabhakaran/Automatic-Fracture-Detection-Code/tree/v1.0.0> (last access: March 30, 2020)
2. The code to modify graphs is available from the following Github repository: <https://github.com/rahulprabhakaran/Fracture-Graph/tree/v1.0.0> (last access: March 5, 2021)

## Data availability

1. The fracture network data presented in this article is available in shapefile, csv, and mat formats on the 4TU data repository associated with this article (<https://doi.org/10.4121/14039234>).
2. The photogrammetric data of the Bristol Channel outcrop used in this article is available at: <http://doi.org/10.18154/RWTH-2020-06903>

## Funding

JLU acknowledges support by the Deutsche Forschungsgemeinschaft (DFG) (grant no. 316167043).

## Author contributions

RP performed the automatic extraction of traces from photogrammetric data, wrote the code to convert shapefiles to graphs and graph modification functions, and wrote the manuscript with inputs from all co-authors. CW acquired the UAV photogrammetric data at the Lilstock outcrop, created the orthomosaics and tiling of images, and contributed to the regional geology section of the manuscript. JU helped acquire the UAV photogrammetric data at the Lilstock outcrop, initiated and organized the collaborative efforts between the universities involved in the project, discussed results, and helped in writing of the manuscript. GB organized the collaboration for the Dutch part of the project, contributed to the development of the methods, discussed the structure and discussion of the results within the manuscript. DS provided funding and

contributed to discussions on the development of methods that are used in and not limited to this manuscript.

## References

- Adler, P.M., Thovert, J.-F., 1999. Fractures and Fracture Networks Volume 15 of Theory and Applications of Transport in Porous Media, first ed. Springer, Dordrecht.
- Andresen, C., Hansen, A., Le Goc, R., Davy, P., Hope, S., 2013. Topology of fracture networks. *Front. Phys.* 1, 7.
- Andrews, B.J., Roberts, J.J., Shipton, Z.K., Bigi, S., Tartarello, M.C., Johnson, G., 2019. How do we see fractures? quantifying subjective bias in fracture data collection. *Solid Earth* 10 (2), 487–516.
- Andrews, B.J., Shipton, Z.K., Lord, R., McKay, L., 2020. The growth of faults and fracture networks in a mechanically evolving, mechanically stratified rock mass: a case study from spireslack surface coal mine, Scotland. *Solid Earth* 11 (6), 2119–2140.
- Barthelemy, M., 2018. Morphogenesis of spatial networks. In: *Lecture Notes in Morphogenesis*, 2018th ed. Springer International Publishing.
- Bastian, M., Heymann, S., Jacomy, M., 2009. Gephi: an Open Source Software for Exploring and Manipulating Networks.
- Belayneh, M., 2004. Palaeostress orientation inferred from surface morphology of joints on the southern margin of the Bristol Channel basin, UK. In: *The Initiation, Propagation, and Arrest of Joints and Other Fractures 1*. Geological Society of London, Special Publications, pp. 243–255.
- Belayneh, M., Cosgrove, J.W., 2004. Fracture-pattern variations around a major fold and their implications regarding fracture prediction using limited data: an example from the Bristol Channel basin. In: *The Initiation, Propagation, and Arrest of Joints and Other Fractures*, vol. 231. Geological Society of London, Special Publications, pp. 89–102, 1.
- Belayneh, M., Geiger, S., Matthai, S.K., 2006. Numerical simulation of water injection into layered fractured carbonate reservoir analogs. *AAPG (Am. Assoc. Pet. Geol.) Bull.* 90 (10), 1473–1493.
- Bemis, S.P., Micklethwaite, S., Turner, D., James, M.R., Akciz, S., Thiele, S.T., Bangash, H.A., 2014. Ground-based and UAV-based photogrammetry: a multi-scale, high-resolution mapping tool for structural geology and paleoseismology. *J. Struct. Geol.* 69 (A), 163–178.
- Berkowitz, B., 2002. Characterizing flow and transport in fractured geological media: a review. *Adv. Water Resour.* 25 (8), 861–884.
- Bertotti, G., Audra, P., Auler, A., Bezerra, F.H., de Hoop, S., Pontes, C., Prabhakaran, R., Lima, R., 2020. The morro vermelho hypogenic karst system (Brazil): stratigraphy, fractures, and flow in a carbonate strike-slip fault zone with implications for carbonate reservoirs. *AAPG (Am. Assoc. Pet. Geol.) Bull.* 104 (10), 2029–2050.
- Bisdom, K., Nick, H., Bertotti, G., 2017. An integrated workflow for stress and flow modelling using outcrop-derived discrete fracture networks. *Comput. Geosci.* 103 (C), 21–35.
- Bistacchi, A., Balsamo, F., Storti, F., Mozafari, M., Swennen, R., Solum, J., Tueckmantel, C., Taberner, C., 2015. Photogrammetric digital outcrop reconstruction, visualization with textured surfaces, and three-dimensional structural analysis and modeling: innovative methodologies applied to fault-related dolomitization (Vajont limestone, southern Alps, Italy). *Geosphere* 11 (6), 2031–2048.
- Boersma, Q., Prabhakaran, R., Bezerra, F.H., Bertotti, G., 2019. Linking natural fractures to karst cave development: a case study combining drone imagery, a natural cave network and numerical modelling. *Petrol. Geosci.* 25 (4), 454–469.
- Bourne, S., Willemsse, E., 2001. Elastic stress control on the pattern of tensile fracturing around a small fault network at Nash Point, UK. *J. Struct. Geol.* 23 (11), 1753–1770.
- Brooks, M., Trayner, P.M., Trimble, T.J., 1988. Mesozoic reactivation of variscan thrusting in the Bristol Channel area, UK. *J. Geol. Soc.* 145 (3), 439–444.
- Bruna, P., Prabhakaran, R., Bertotti, G., Straubhaar, J., Plateaux, R., Maerten, L., Mariethoz, G., Meda, M., 2019a. The mps-based fracture network simulation method: application to subsurface domain. In: *11th EAGE Conference and Exhibition, London 2019*, pp. 1–5, 2019.
- Bruna, P.-O., Straubhaar, J., Prabhakaran, R., Bertotti, G., Bisdom, K., Mariethoz, G., Meda, M., 2019b. A new methodology to train fracture network simulation using multiple-point statistics. *Solid Earth* 10 (2), 537–559.
- Csardi, G., Nepusz, T., 2006. The Igraph Software Package for Complex Network Research. *InterJournal, Complex Systems*, p. 1695.
- Dart, C.J., McClay, K., Hollings, P.N., 1995. 3d analysis of inverted extensional fault systems, southern Bristol Channel basin, UK. *Geol. Soc. London, Special Publ.* 88 (1), 393–413.
- Day-Lewis, F.D., Slater, L.D., Robinson, J., Johnson, C.D., Terry, N., Werkema, D., 2017. An overview of geophysical technologies appropriate for characterization and monitoring at fractured-rock sites. *J. Environ. Manag.* 204 (Part 2), 709–720.
- De Berg, M., Van Kreveld, M., Overmars, M., Schwarzkopf, O.C., 2000. *Computational Geometry. Algorithms and Applications*. Springer, Berlin, Heidelberg.
- Dershowitz, W.S., Herda, H.H., 1992. Interpretation of Fracture Spacing and Intensity. The 33rd U.S. Symposium on Rock Mechanics (USRMS). Santa Fe, New Mexico, June 1992.
- Engelder, T., Peacock, D.C., 2001. Joint development normal to regional compression during flexural-flow folding: the Lilstock buttress anticline, Somerset, England. *J. Struct. Geol.* 23 (2), 259–277.
- Gillespie, P., Monsen, E., Maerten, L., Hunt, D., Thurmond, J., Tuck, D., 2011. Fractures in carbonates: from digital outcrops to mechanical models. In: *Outcrops Revitalized: Tools, Techniques and Applications*. SEPM Society for Sedimentary Geology.

- Glen, R., Hancock, P., Whittaker, A., 2005. Basin inversion by distributed deformation: the southern margin of the bristol channel basin, england. *J. Struct. Geol.* 27 (12), 2113–2134.
- Guo, L., Latham, J.-P., Xiang, J., 2017. A numerical study of fracture spacing and through-going fracture formation in layered rocks. *Int. J. Solid Struct.* 110–111, 44–57.
- Hagberg, A.A., Schult, D.A., Swart, P.J., 2008. Exploring network structure, dynamics, and function using networkx. In: Varoquaux, G., Vaught, T., Millman, J. (Eds.), *Proceedings of the 7th Python in Science Conference*, pp. 11–15 (Pasadena, CA USA).
- Hancock, P., Engelder, T., 1989. Neotectonic joints. *GSA Bull.* 101 (10), 1197–1208.
- Hanke, J.R., Fischer, M.P., Pollyea, R.M., 2018. Directional semivariogram analysis to identify and rank controls on the spatial variability of fracture networks. *J. Struct. Geol.* 108, 34–51. Spatial arrangement of fractures and faults.
- Healy, D., Rizzo, R.E., Cornwell, D.G., Farrell, N.J., Watkins, H., Timms, N.E., Gomez-Rivas, E., Smith, M., 2017. Fracpaq: a matlab™ toolbox for the quantification of fracture patterns. *J. Struct. Geol.* 95, 1–16.
- Hodgetts, D., 2013. Laser scanning and digital outcrop geology in the petroleum industry: a review. *Mar. Petrol. Geol.* 46, 335–354.
- Kamerling, P., 1979. The geology and hydrocarbon habitat of the bristol channel basin. *J. Petrol. Geol.* 2 (1), 75–93.
- Kelly, P., Peacock, D., Sanderson, D., McGurk, A., 1999. Selective reverse-reactivation of normal faults, and deformation around reverse-reactivated faults in the mesozoic of the somerset coast. *J. Struct. Geol.* 21 (5), 493–509.
- Lamarche, J., Borgomano, J., Caline, B., Gisquet, F., Rigaud, S., Schröder, S., Viseur, S., Martinsen, O.J., Pulham, A.J., Haughton, P.D.W., Sullivan, M.D., 2011. Characterization of Fault-Related Dolomite Bodies in Carbonate Reservoirs Using Lidar Scanning.
- Laubach, S.E., Lander, R.H., Criscenti, L.J., Anovitz, L.M., Urai, J.L., Pollyea, R.M., Hooker, J.N., Narr, W., Evans, M.A., Kerisit, S.N., Olson, J.E., Dewers, T., Fisher, D., Bodnar, R., Evans, B., Dove, P., Bonnell, L.M., Marder, M.P., Pyrak-Nolte, L., 2019. The role of chemistry in fracture pattern development and opportunities to advance interpretations of geological materials. *Rev. Geophys.* 57 (3), 1065–1111.
- Lavoine, E., Davy, P., Darcel, C., Munier, R., 2020. A discrete fracture network model with stress-driven nucleation: impact on clustering, connectivity, and topology. *Front. Phys.* 8, 9.
- Lepillier, B., Yoshioka, K., Parisio, F., Bakker, R., Bruhn, D., 2020. Variational phase-field modeling of hydraulic fracture interaction with natural fractures and application to enhanced geothermal systems. *J. Geophys. Res.: Solid Earth* 125 (7), e2020JB019856.
- Loosveld, R.J.H., Franssen, R.C.M.W., 1992. Extensional vs. shear fractures: implications for reservoir characterisation. In: *European Petroleum Conference, Cannes, France. European Petroleum Conference, Cannes, France Society of Petroleum Engineers*, p. 8.
- Manzocchi, T., 2002. The connectivity of two-dimensional networks of spatially correlated fractures. *Water Resour. Res.* 38 (9), 1–1–1–20.
- Mauldon, M., Dunne, W., Rohrbach, M., 2001. Circular scanlines and circular windows: new tools for characterizing the geometry of fracture traces. *J. Struct. Geol.* 23 (3), 247–258.
- Molron, J., Linde, N., Baron, L., Selroos, J.-O., Darcel, C., Davy, P., 2020. Which fractures are imaged with ground penetrating radar? results from an experiment in the Åspö hardrock laboratory, Sweden. *Eng. Geol.* 273, 105674.
- National Research Council, 1996. *Rock Fractures and Fluid Flow: Contemporary Understanding and Applications*, 1996th ed. The National Academies Press, Washington, DC. Washington, DC.
- Nemčok, M., Gayer, R., Milliorizos, M., 1995. Structural analysis of the inverted bristol channel basin: implications for the geometry and timing of fracture porosity. In: *Basin Inversion*, vol. 88. The Geological Society, London, pp. 355–392.
- Nishizeki, T., Rahman, M., 2004. *Planar Graph Drawing*. World Scientific Publishing.
- Nyberg, B., Nixon, C.W., Sanderson, D.J., 2018. NetworkGT: a GIS tool for geometric and topological analysis of two-dimensional fracture networks. *Geosphere* 14 (4), 1618–1634.
- Odling, N.E., 1997. Scaling and connectivity of joint systems in sandstones from western Norway. *J. Struct. Geol.* 19 (10), 1257–1271.
- Palamakumbura, R., Krabbendam, M., Whitbread, K., Arnhardt, C., 2020. Data acquisition by digitizing 2-d fracture networks and topographic lineaments in geographic information systems: further development and applications. *Solid Earth* 11 (5), 1731–1746.
- Passchier, M., Passchier, C.W., Weismüller, C., Urai, J.L., 2021. The joint sets on the lilstock benches, UK. observations based on mapping a full resolution uav-based image. *J. Struct. Geol.* 147, 104332.
- Peacock, D., Sanderson, D., Bastesen, E., Rotevatn, A., Storstein, T., 2019. Causes of bias and uncertainty in fracture network analysis. *Norw. J. Geol.* 99 (1), 113–128.
- Peacock, D., Sanderson, D., Rotevatn, A., 2018. Relationships between fractures. *J. Struct. Geol.* 106, 41–53.
- Peacock, D.C.P., 2004. Differences between veins and joints using the example of the jurassic limestones of somerset. In: *The Initiation, Propagation, and Arrest of Joints and Other Fractures*, vol. 231. Geological Society of London, Special Publications, pp. 209–221.
- Philip, Z.G., Jennings, J.W., Olson, J.E., Laubach, S.E., Holder, J., 2005. Modeling coupled fracture-matrix fluid flow in geomechanically simulated fracture networks. *SPE Reservoir Eval. Eng.* 8 (4), 300–309.
- Potts, G.J., Reddy, S.M., 2000. Application of younging tables to the construction of relative deformation histories—1: fracture systems. *J. Struct. Geol.* 22 (10), 1473–1490.
- Prabhakaran, R., 2019. *Rahulprabhakaran/Automatic-Fracture-Detection- Code* (supplement to Solid Earth Manuscript Se-2019-104).
- Prabhakaran, R., Bruna, P.-O., Bertotti, G., Smeulders, D., 2019. An automated fracture trace detection technique using the complex shearlet transform. *Solid Earth* 10 (6), 2137–2166.
- Priest, S., Hudson, J., 1981. Estimation of discontinuity spacing and trace length using scanline surveys. *Int. J. Rock Mech. Min. Sci. Geomech. Abstr.* 18 (3), 183–197.
- Procter, A., Sanderson, D.J., 2018. Spatial and layer-controlled variability in fracture networks. *J. Struct. Geol.* 108, 52–65. Spatial arrangement of fractures and faults.
- Rawnsley, K., Peacock, D., Rives, T., Petit, J.-P., 1998. Joints in the mesozoic sediments around the bristol channel basin. *J. Struct. Geol.* 20 (12), 1641–1661.
- Reisenhofer, R., Kiefer, J., King, E.J., 2016. Shearlet-based detection of flame fronts. *Exp. Fluid* 57, 41.
- Remij, E.W., Remmers, J.J.C., Pizzocolo, F., Smeulders, D.M.J., Huyghe, J.M., 2015. A partition of unity-based model for crack nucleation and propagation in porous media, including orthotropic materials. *Transport Porous Media* 106 (3), 505–522.
- Rohrbaugh Jr., M.B., Dunne, W.M., Mauldon, M., 2002. Estimating fracture trace intensity, density, and mean length using circular scan lines and windows. *AAPG (Am. Assoc. Pet. Geol.) Bull.* 86, 2089–2104.
- Sanderson, D.J., Nixon, C.W., 2015. The use of topology in fracture network characterization. *J. Struct. Geol.* 72, 55–66.
- Sanderson, D.J., Peacock, D.C., Nixon, C.W., Rotevatn, A., 2019. Graph theory and the analysis of fracture networks. *J. Struct. Geol.* 125, 155–165, 40th Anniversary Special Issue “Back to the Future: 40 years of Structural Geology and beyond”.
- Santiago, E., Velasco-Hernández, J.X., Romero-Salcedo, M., 2016. A descriptive study of fracture networks in rocks using complex network metrics. *Comput. Geosci.* 88, 97–114.
- Scott, D.N., Wohl, E.E., 2019. Bedrock fracture influences on geomorphic process and form across process domains and scales. *Earth Surf. Process. Landforms* 44 (1), 27–45.
- Snyder, M.E., Waldron, J.W., 2018. Fracture overprinting history using Markov chain analysis: windsor-kennetcook subbasin, maritimes basin, Canada. *J. Struct. Geol.* 108, 80–93 (Special Issue: Spatial arrangement of fractures and faults).
- Spruzeniec, L., Späth, M., Urai, J.L., Ukar, E., Selzer, M., Nestler, B., Schwed, A., 2020. Formation of wide-blocky calcite veins by extreme growth competition. *J. Geol. Soc.* 178 (2), jgs2020-j2104.
- Thovet, J.-F., Mourzenko, V., Adler, P., 2017. Percolation in three-dimensional fracture networks for arbitrary size and shape distributions. *Phys. Rev.* 95 (4), 042112.
- Ukar, E., Laubach, S.E., Hooker, J.N., 2019. Outcrops as guides to subsurface natural fractures: example from the nikanassin formation tight-gas sandstone, grande cache, alberta foothills, Canada. *Mar. Petrol. Geol.* 103, 255–275.
- Valentini, L., Perugini, D., Poli, G., 2007a. The ‘small-world’ nature of fracture/conduit networks: possible implications for disequilibrium transport of magmas beneath mid-ocean ridges. *J. Volcanol. Geoth. Res.* 159 (4), 355–365.
- Valentini, L., Perugini, D., Poli, G., 2007b. The ‘small-world’ topology of rock fracture networks. *Phys. Stat. Mech. Appl.* 377 (1), 323–328.
- Valliappan, V., Remmers, J.J.C., Barnhoorn, A., Smeulders, D.M.J., 2019. A numerical study on the effect of anisotropy on hydraulic fractures. *Rock Mech. Rock Eng.* 52 (2), 591–609.
- Van Hoon, B., 1987. The south celtic sea/bristol channel basin: origin, deformation and inversion history. *Tectonophysics* 137 (1), 309–334 (Special Issue: Compressional Intra-Plate Deformations in the Alpine Foreland).
- Vevatne, J.N., Rimstad, E., Hope, S.M., Korsnes, R., Hansen, A., 2014. Fracture networks in sea ice. *Front. Phys.* 2, 21.
- Virgo, S., Abe, S., Urai, J.L., 2016. The influence of loading conditions on fracture initiation, propagation, and interaction in rocks with veins: results from a comparative discrete element method study. *J. Geophys. Res.: Solid Earth* 121 (3), 1730–1738.
- Watts, D.J., Strogatz, S.H., 1998. Collective dynamics of ‘small-world’ networks. *Nature* 393, 440–442.
- Weismüller, C., Passchier, M., Urai, J., Reicherter, K., 2020a. The Fracture Network in the Lilstock Pavement, Bristol Channel, uk: Digital Elevation Models and Orthorectified Mosaics Created from Unmanned Aerial Vehicle Imagery. RWTH Publications.
- Weismüller, C., Prabhakaran, R., Passchier, M., Urai, J.L., Bertotti, G., Reicherter, K., 2020b. Mapping the fracture network in the lilstock pavement, bristol channel, UK: manual versus automatic. *Solid Earth* 11 (5), 1773–1802.
- Welch, M.J., Luthje, M., Glad, A.C., 2019. Influence of fracture nucleation and propagation rates on fracture geometry: insights from geomechanical modelling. *Petrol. Geosci.* 25 (4), 470–489. Thematic Collection: Naturally Fractured Reservoirs.
- Wilson, C.E., Aydin, A., Karimi-Fard, M., Durlifsky, L.J., Amir, S., Brodsky, E.E., Kreylos, O., Kellogg, L.H., 2011. From outcrop to flow simulation: constructing discrete fracture models from a lidar survey. *AAPG (Am. Assoc. Pet. Geol.) Bull.* 95 (11), 1883–1905.
- Wüstefeld, P., 2010. Capturing a World-Class Outcrop of a Quality Calcite Vein Network on a Polish Limestone Outcrop in the oman Mountains: Creation of a High Resolution Panorama and Microstructural Vein Description.
- Wyller, F.A., 2019. Spatio-temporal Development of a Joint Network and its Properties: a Case Study from Lilstock uk.
- Yoshioka, K., Bourdin, B., 2016. A variational hydraulic fracturing model coupled to a reservoir simulator. *Int. J. Rock Mech. Min. Sci.* 88, 137–150.